Research Square

Preprints are preliminary reports that have not undergone peer review.
They should not be considered conclusive, used to inform clinical practice,
or referenced by the media as validated information.

An Open Nonequilibrium Effective Quantum Field Formulation of the Corneal High Entropy-Production Zone

Yasushi Sonoda

sonodayasushi@gmail.com

Mejiro Dori Clinic https://orcid.org/0009-0009-6784-0323

Research Article

Keywords: High Entropy-Production Zone (HEZ), corneal stroma, open quantum field theory, nonequilibrium quantum field theory, Schwinger–Keldysh formalism, Lindblad field dynamics, entropy production, quantum decoherence, Marangoni-like transport, dissipative structure, corneal transparency, information redistribution, Endothelial/HEZ Transport Index (EHTI), Dissipative Decoherence Structure (DDS)

Posted Date: November 19th, 2026

DOI: https://doi.org/10.21203/rs.3.rs-11771793/v1

License: This work is licensed under a Creative Commons Attribution 4.0 International License.
Read Full License

Additional Declarations: The authors declare no competing interests.

An Open Nonequilibrium Effective Quantum Field Formulation of the Corneal High Entropy-Production Zone

Yasushi Sonoda

Mejiro Dori Clinic, Tokyo, Japan

ORCID: 0009-0009-6784-0323

Abstract

The cornea maintains transparency through nonequilibrium regulation of hydration, solute transport, and collagen organization. The High Entropy-Production Zone (HEZ) hypothesis proposes that spatially organized dissipation in the anterior stroma may couple microscopic relaxation to useful gradient-driven transport. We reformulated this hypothesis as a spatially resolved open nonequilibrium effective quantum field theory linking a coarse-grained hydration/proton collective field and collagen order with classical solute and temperature variables. Local Lindblad channels and Schwinger–Keldysh kernels provided a formal description of dissipation, response, fluctuations, and correlations, while Marangoni-like transport coupling remained phenomenological. The conceptual HEZ was represented as an anteriorly biased, quasi-two-dimensional dissipative field without a fixed anatomical depth. We distinguished Spohn-type relative-entropy relaxation from physical entropy production and introduced a classical flux–affinity entropy-production expression, a connected density-correlation observable, and prospective transport-efficiency measures, including the Endothelial/HEZ Transport Index (EHTI) and a localization-dependent gain functional. In illustrative local-Markovian calculations using a prescribed Gaussian reference profile, increased damping produced broader spectral linewidths and shorter first-order field-amplitude correlation times. At the imposed 70-μm reference center, their normalized values were 2.0 and 0.5, respectively. Lorentzian and geometry-sensitivity analyses confirmed the dependence of these responses on the assumed damping relation and spatial profile. Despite identical depth-integrated excess damping, anterior, uniform, and posterior control profiles produced distinct local spectral and temporal signatures, demonstrating the importance of spatial organization within the specified model. These findings provide conditional observables and reproducible benchmarks for future quantitative investigation of a Dissipative Decoherence Structure (DDS), in which microscopic decoherence-associated information redistribution may become functionally coupled to macroscopic transport. However, the calculations did not independently establish HEZ localization, increased physical entropy production, corneal quantum decoherence, or DDS function. The resulting formulation offers a testable theoretical basis for investigating spatially organized dissipation and its possible relationship to useful transport. Future studies must identify relevant collective modes, obtain depth-resolved spectral and correlation measurements, independently quantify physical entropy production and transport, and reconstruct spatial organization without imposing a predefined HEZ geometry.

Keywords: High Entropy-Production Zone (HEZ), corneal stroma, open quantum field theory, nonequilibrium quantum field theory, Schwinger–Keldysh formalism, Lindblad field dynamics, entropy production, quantum decoherence, Marangoni-like transport, dissipative structure, corneal transparency, information redistribution, Endothelial/HEZ Transport Index (EHTI), Dissipative Decoherence Structure (DDS)

Introduction

Biological tissues maintain order under nonequilibrium conditions while exchanging matter and energy with the environment. Corneal transparency likewise depends on the regulation of stromal hydration, collagen organization, solute transport, and boundary fluxes, and even small disturbances can alter optical properties. Conventional explanations have emphasized endothelial pump–leak balance, osmotic pressure, diffusion, swelling pressure, and lamellar structure [1–3]. In an earlier report, the author introduced the HEZ hypothesis as a nonequilibrium model in which high entropy production within a localized anterior stromal region links solute and temperature gradients to organized transport [4]. In this paper, the HEZ is defined as an anteriorly biased, anisotropic, Gaussian-like quasi-two-dimensional dissipative field with a maximum immediately beneath Bowman's layer and continuous decay toward the endothelium and from the center toward the periphery (Figure 1). $x_0 = 70$ μm, σ = 40 μm, and 50–100 μm are simulation reference values used for comparison with the previous model and are not fixed anatomical definitions. In a subsequent report, the author extended the HEZ hypothesis by reconstructing it as a localized open quantum subsystem in which water–collagen interactions and proton transport were represented by a two-level model, environmental coupling by Lindblad dynamics, and entropy production by von Neumann entropy and Spohn's inequality [5]. In that previous study, we also tentatively used the term "Dissipative Decoherence Structure" (DDS) to describe a hypothesized connection between microscopic decoherence-associated dissipation and macroscopic stromal organization [5]. The Lindblad and quantum-thermodynamic methods used in that extension have established theoretical foundations [6, 7]. The purpose was to examine whether the internal consistency of the HEZ could be maintained after quantum-information-theoretic dissipation was added to the classical description. However, a single reduced density matrix cannot naturally treat spatial correlations, collective modes, correlation lengths, local spectral responses, or depth-dependent dissipation. Describing the HEZ as a spatially extended dissipative structure requires extension of the finite-dimensional subsystem to an effective quantum field with position-dependent degrees of freedom. Nonrelativistic quantum field theory is widely used in condensed-matter and statistical physics to describe collective excitations, transport, order parameters, and many-body systems. For nonequilibrium open systems, the Schwinger–Keldysh formalism provides a unified description of response, fluctuations, noise, and dissipation, and Lindblad dynamics can likewise be generalized to local field operators [8–12]. Even under strong decoherence, correlation and response functions remain useful observables. Accordingly, this study reformulates the HEZ hypothesis as an open nonequilibrium effective quantum field theory. The field $\widehat{\Psi}(\mathbf{x}, t)$ introduced below should not be interpreted as a claim that the entire cornea forms a phase-coherent quantum condensate. Rather, it is a coarse-grained field representing collective hydration/proton degrees of freedom that remain after short-range microscopic modes have been integrated out. Corneal tissue is warm, water-rich, heterogeneous, and strongly coupled to the environment. Strong decoherence is not an obstacle to this formulation; it is incorporated into the theory as a spatially varying dissipative kernel. Here, information dissipation means a reduction in locally accessible coherence or distinguishability. If the full system is regarded as part of a larger closed system, information need not be destroyed but may be redistributed into environmental degrees of freedom or system–environment correlations. Furthermore, the goals of this reformulation are to extend the HEZ into a spatially resolved dissipative field, define observables such as response, correlations, linewidth, correlation time, and local entropy production, establish a reduction relation to classical transport, and generalize the EHTI using field-theoretic methods. The central question is whether a localized dissipative-field kernel can preserve the transport hierarchy of the original model while generating new spatial and correlation-based predictions. If so, the HEZ can be represented as a field region in which the coupling among thermodynamic gradients, environmental dissipation, collective correlations, and transport is locally enhanced. An additional motivation for the present field-theoretic extension was to make the previously proposed DDS amenable to future quantitative analysis. Here, DDS was not defined by enhanced microscopic decoherence alone; it denoted the testable possibility that spatially organized loss of locally accessible coherence and redistribution into environmental correlations could be functionally coupled, after coarse-graining, to useful hydration or solute transport. Its evaluation would therefore require

more than a locally increased damping rate or a shortened first-order correlation time. Relevant future tests would need independently identified collective modes, depth-resolved response and fluctuation measurements, correlation dynamics, a calibrated physical entropy-production budget, and evidence for an effective stress–transport or other justified transport coupling. The purpose of the present work was to establish candidate observables and controlled reference calculations for such a program, while leaving DDS function, quantum discord, correlation memory, and transport enhancement unproven. In particular, geometry-independent reconstruction would be necessary to distinguish a recovered spatial organization from an imposed anterior Gaussian reference profile.

Methods

We reformulated the HEZ hypothesis as a spatially resolved open nonequilibrium effective quantum field theory, incorporating local Lindblad channels, Schwinger–Keldysh response and noise, a Spohn-type relaxation diagnostic, phenomenological Marangoni-like coupling, correlation observables, and the operational EHTI. The numerical work evaluated an imposed Gaussian reference kernel (Figure 2), its local-Markovian linewidth and correlation-time responses (Figure 3), an equal-area Lorentzian illustration (Figure 4), a geometry-sensitivity sweep (Figure 5), and a matched-integrated-excess-damping spatial control (Figure 6). These deterministic exercises used prescribed coefficients and geometry, without fitting corneal data, solving full quantum-field evolution, calculating physical entropy production, or simulating stromal flow or DDS function. The methods used were summarized in Table 1. AI assistance (ChatGPT (OpenAI; GPT-6)) was used for mathematical formulation, editorial revision, and illustrative numerical postprocessing. Reproduction instructions for Figures 2–5 and Table 3 are provided in Supplementary Section S8; the matched-integrated-excess-damping control of Figure 6 is specified in Section S7.

1. HEZ Model Scope and Reference Geometry

Elements inherited from the prior model were: (i) a corneal stromal thickness of approximately 450 μm; (ii) a one-dimensional Gaussian kernel with center $x_0 = 70$ μm and characteristic width $\sigma = 40$ μm, treated as a "simulation reference geometry" distinct from the conceptual definition of the HEZ; (iii) solute and temperature gradients as external nonequilibrium driving forces; (iv) a qualitative hierarchy in which the solutal contribution is stronger than the thermal contribution in the effective Marangoni-like driving; (v) a thermal-stabilization channel; (vi) baseline dephasing and energy-relaxation rates of $10^3\ \mathrm{s}^{-1}$ and $10^2\ \mathrm{s}^{-1}$, respectively, adopted in Reference 5 as illustrative simulation parameters rather than experimentally measured corneal rates and retained here solely as phenomenological reference scales; and (vii) an entropy-normalized transport efficiency as a cross-scale index. Newly introduced elements were field degrees of freedom, spatially local dissipators, Keldysh response and noise functions, local entropy-production density, and field-corrected interfacial free energy. Coupling constants that could not be directly inherited from the prior model were left symbolic, and unmeasured quantities were not treated as if they were experimental values. Thus, the present study did not derive corneal physiology from first principles; rather, it organized the couplings permitted within a coarse-grained effective field theory. These coefficients must ultimately be constrained by future experiments or more microscopic calculations. We explicitly separated the conceptual definition of the HEZ from its numerical parameterization. We defined the HEZ as an anteriorly biased, anisotropic, Gaussian-like quasi-two-dimensional dissipative field, assuming a maximum of local entropy production immediately beneath Bowman's layer and continuous decay toward the endothelium and from the center toward the periphery. No sharp anatomical boundary was assumed.

We assumed a quasi-holographic character of the HEZ, but the term "quasi-holographic" was used as a thermodynamic metaphor to express functional projection or encoding of the three-dimensional stromal state onto an anteriorly biased quasi-two-dimensional field. $x_0 = 70$ μm, σ = 40 μm, and 50–100 μm were all simulation reference values for comparison and reproducibility, not fixed positions or widths of the HEZ, measured values, or first-principles predictions. The stroma was first represented as a one-dimensional slab along the depth coordinate $x \in [0, L]$, with $L = 450$ μm. The anterior stromal surface was defined as $x = 0$, and the posterior boundary was placed near $x = L$. Extension to two or three dimensions is straightforward in principle and would be required for a quantitative treatment of lateral vortex formation, but a one-dimensional depth profile was used here to preserve direct correspondence with the original model. To implement the conceptual definition above in the one-dimensional numerical model, the following dimensionless localization field was used as the simulation reference kernel. Figure 1 summarized the conceptual spatial organization of the HEZ.

$$\phi_{\mathrm{HEZ}}(x) = A_{\mathrm{HEZ}} \exp\left[-\frac{(x-x_0)^2}{2\sigma^2}\right], \tag{1}$$

Here $A_{\mathrm{HEZ}} = 1$, $x_0 = 70$ μm, and $\sigma = 40$ μm. $x_0 = 70$ μm and σ = 40 μm were baseline values inherited from the previous model and were consistently termed the "simulation reference geometry" in this paper. They were not treated as the conceptual definition of the HEZ, a fixed anatomical position, boundary, or width, an intrinsically measured dimension, or a first-principles QFT prediction. The function in Eq. (1) itself does not represent entropy. Rather, it was used as a spatial weighting function for dissipative couplings, field–matter couplings, and the entropy-production kernel. In a three-dimensional formulation, the same profile can be multiplied by a slowly varying lateral envelope $f(r_{\parallel})$ when a center-to-periphery gradient is required. We performed an illustrative numerical profile simulation for Figure 2 by evaluating the imposed, dimensionless Gaussian kernel φ_HEZ(x) in Eq. (1) over the 0–450 μm stromal depth using the inherited reference center of 70 μm and width of 40 μm. We plotted the resulting normalized profile in Figure 2.

2. Open Effective Quantum-Field Dynamics

The finite-dimensional two-level subsystem was replaced by a nonrelativistic bosonic field operator $\hat{\Psi}(\mathbf{x}, t)$ representing a coarse-grained collective hydration/proton excitation sector. Because the available information does not uniquely identify the microscopic quasiparticle, this interpretation was deliberately kept broad. Depending on future experimental constraints, $\hat{\Psi}$ may represent an effective proton-polarization mode, a hydration-network excitation, or another collective degree of freedom coupled to collagen organization or local solute composition. To describe slowly varying structural order in the stroma, a real collagen-order field $\chi(\mathbf{x}, t)$ was introduced. In the minimal implementation, χ was treated semiclassically, although it could be promoted to a quantum field if justified by the relevant scale and measurements. A local number-operator-like observable for the collective field was defined as follows.

$$\hat{n}(\mathbf{x}) = \hat{\Psi}^{\dagger}(\mathbf{x})\hat{\Psi}(\mathbf{x}). \tag{2}$$

The microscopic field identity was left open. Hydration-shell, hydrogen-bond, proton-coupled, and collagen–water vibrational degrees of freedom were considered only as candidate microscopic contexts. References [13–15] provide general quantum-biology background. Field-theoretic entropy-production work was used only as a structural precedent [16–18], not as corneal numerical input. The field theory was defined at a finite coarse-graining scale a, corresponding to an ultraviolet momentum cutoff Λ of order 1/a. This regularization was introduced to avoid the formal singularities of local Lindblad operators and contact interactions in the continuum limit. In an actual discretization, a may be identified with the spatial lattice spacing, but it should not be interpreted as a fundamental microscopic length. Throughout the dissipative sector, a denotes the coarse-graining length, while dissipative-channel labels are denoted c to avoid notational ambiguity. With the continuum normalization $[\Psi(x), \Psi^{\dagger}(x')] = \delta^3(x-x')$, Ψ has dimensions $L^{-3/2}$; this normalization was used for the Lindblad-operator dimensional regularization. Notation convention: the Gaussian amplitude is AHEZ and its center is x_0 (the width remains σ); the spectral function is AΨ; mode labels A and B in Eqs. (31–32), and generic observables A and B in Eq. (33), are contextual labels rather than Gaussian amplitudes or spectra. Entropy-production densities σq and σcl are distinguished by subscripts from Gaussian width σ, while τM denotes tangential stress and τΨ denotes the first-order field-amplitude correlation time.

The conservative part of the theory was described as follows.

$$\hat{H}_{\mathrm{EFT}} = \int d^3x \left[\hat{\Psi}^{\dagger}\left(-\frac{\hbar^2\nabla^2}{2m_{\mathrm{eff}}} + U_{\mathrm{eff}}(\mathbf{x}, t) - \mu_{\mathrm{eff}}\right)\hat{\Psi} + \frac{u}{2}\hat{\Psi}^{\dagger}\hat{\Psi}^{\dagger}\hat{\Psi}\hat{\Psi} + \frac{\kappa_{\chi}}{2}|\nabla\chi|^2 + V_{\chi}(\chi)\right], \tag{3}$$

$$U_{\mathrm{eff}} = g_{\chi}\chi + g_C\,[C - C_0] + g_T\,[T - T_0] + g_H\phi_{\mathrm{HEZ}}(x). \tag{4}$$

Here m_{eff} is an effective mass or stiffness parameter, μ_{eff} is an effective chemical potential, u is a local interaction coefficient, g_{χ} couples the collective field to stromal order, and g_C, g_T, and g_H represent couplings to the solute field, temperature field, and HEZ localization profile, respectively. Because the original model does not constrain these new coefficients, no numerical values were assigned to them in this

paper. The collagen-order potential in Eq. (3) was treated as a generic Landau-type term, subject to the stability conditions stated below; its coefficients were not calibrated. For definiteness, an illustrative Landau potential is $V_\chi(\chi) = (r_\chi/2)\chi^2 + (v_\chi/4)\chi^4 - h_\chi\chi$, with $v_\chi > 0$ for quartic stability. The phenomenological coefficients r_χ, v_χ, and h_χ are those listed in Table S3; this choice does not imply that their values or the polynomial truncation have been established for corneal collagen. Environmental coupling was then introduced through the following field-generalized Lindblad equation, using standard open-system and field-Lindblad formulations [6, 9].

$$\frac{d\rho}{dt} = -\frac{i}{\hbar}\left[\widehat{H}_{\mathrm{EFT}}, \rho\right] + \int d^3x \sum_c \mathcal{D}\left[\hat{L}_c(\mathbf{x})\right]\rho, \tag{5}$$

where

$$\mathcal{D}\left[\hat{L}\right]\rho = \hat{L}\rho\hat{L}^\dagger - \frac{1}{2}\{\hat{L}^\dagger\hat{L}, \rho\}. \tag{6}$$

Three representative local channels were introduced.

$$\hat{L}_\phi(\mathbf{x}) = \sqrt{\Gamma_\phi(\mathbf{x}, t)\, a^3}\, \hat{n}(\mathbf{x}), \tag{7}$$

$$\hat{L}_{\mathrm{loss}}(\mathbf{x}) = \sqrt{\Gamma_{\mathrm{loss}}(\mathbf{x}, t)}\, \widehat{\Psi}(\mathbf{x}), \tag{8}$$

$$\hat{L}_{\mathrm{gain}}(\mathbf{x}) = \sqrt{\Gamma_{\mathrm{gain}}(\mathbf{x}, t)}\, \widehat{\Psi}^\dagger(\mathbf{x}). \tag{9}$$

The first channel represented local phase randomization, i.e. dephasing. The second and third represented effective loss/relaxation to the environment and gain/injection from the environment, respectively. The precise microscopic interpretation of these operators ultimately depends on how $\widehat{\Psi}$ is identified. In this formulation they were used as the minimal Markov channels required to represent loss of local phase information, relaxation, and nonequilibrium driving. Each rate was spatially modulated. For the density-type dephasing channel, the factor a^3 inside the square root regularized the operator at the finite coarse-graining volume a^3, so Γ_ϕ retains the dimensions of an inverse time under the continuum normalization above. The loss and gain channels already have the corresponding continuum dimensions.

$$\Gamma_c(\mathbf{x}, t) = \Gamma_{c,0} + \lambda_c^C \mathcal{F}_C[\nabla C] + \lambda_c^T \mathcal{F}_T[\nabla T] + \lambda_c^H \phi_{\mathrm{HEZ}}(x), \tag{10}$$

Here $\mathcal{F}_C$ and $\mathcal{F}_T$ are nonnegative scalar functions of the local gradients. Simple choices are the magnitudes $|\nabla C|$ and $|\nabla T|$ (or their squared magnitudes), but these may be replaced by more realistic nonnegative constitutive functions. The channel index $c \in \{\phi, \mathrm{loss}, \mathrm{gain}\}$ is not a solute-species label. The composite solutal contribution to the effective linewidth is instead denoted Γ_{sol} in Eq. (28).

For the minimal local three-channel Markov model, we expressed the first-moment linewidth entering the retarded propagator in terms of the local channels as follows:

$$\Gamma_{\mathrm{eff}}(\mathbf{x}, t) = \Gamma_{\mathrm{loss}}(\mathbf{x}, t) - \Gamma_{\mathrm{gain}}(\mathbf{x}, t) + \Gamma_\phi(\mathbf{x}, t). \tag{11}$$

Thus dephasing contributes to coherence decay and spectral broadening but not directly to number relaxation. Additional interaction- or self-energy-induced broadening, if included in a more complete model, would add to the minimal effective linewidth in Eq. (11). Solutal dominance and possible thermal stabilization were retained as phenomenological constraints, rather than independently predicted or calibrated properties. GKLS admissibility required nonnegative spatially and temporally modulated channel rates in the complete parameter domain. The minimal linear bosonic sector required loss greater than gain for a normalizable stationary occupation and positive effective damping for the stable retarded propagator. These were model admissibility conditions, not measured inequalities in corneal tissue. The

coarse-grained Hamiltonian was assumed bounded from below under a finite ultraviolet cutoff and suitable interaction and collagen-order stability conditions.

3. Schwinger–Keldysh Response and Noise

To describe response and noise, we used a quadratic Schwinger–Keldysh representation with the symmetric rotation Ψ_cl = (Ψ_+ + Ψ_−)/√2 and Ψ_q = (Ψ_+ − Ψ_−)/√2 (so Ψ_cl = √2 Ψ on the physical contour) [8, 12]. We treated the following kernel as a Gaussian/linearized approximation, not as an exact action for all nonlinear Lindblad channels.

$$S_K^{(2)} = \int_{\omega,\mathbf{k}} \left[\Psi_q^* P^R \Psi_{cl} + \Psi_{cl}^* P^A \Psi_q + \Psi_q^* P^K \Psi_q\right]. \tag{12}$$

For the complex bosonic field, the superscript * in Eq. (12) denotes complex conjugation. The displayed frequency–momentum integral is a local/Wigner shorthand evaluated at a slowly varying center position and time; an explicitly inhomogeneous treatment requires the corresponding bilocal position–time kernels. The Gaussian inverse-noise component P^K must be fixed consistently with the same finite-cutoff Lindblad generator (or a specified influence functional), rather than inferred from Γeff alone.

Here $P^R = (G^R)^{-1}$ and $P^A = (G^A)^{-1}$, while $P^K = [G^{-1}]^K$ denotes the Keldysh/noise component of the inverse Green-function kernel; it should not be read as the reciprocal of G^K. For a locally Markovian damped mode, the retarded propagator was approximated in the following form.

$$G^R(\mathbf{k}, \omega; \mathbf{x}) \simeq \left[\hbar\omega - \varepsilon_{\mathbf{k}} - U_{\text{eff}}(\mathbf{x}) + \mu_{\text{eff}} + i\,\frac{\hbar\Gamma_{\text{eff}}(\mathbf{x})}{2}\right]^{-1}. \tag{13}$$

Under the angular-frequency convention used in Eq. (13), Γeff is the full width at half maximum (FWHM) of the simple Lorentzian response, while the half-width at half maximum (HWHM) is Γeff/2. The associated first-order field-amplitude decay time is $\tau_\Psi \simeq 2/\Gamma_{\text{eff}}$. These relations follow from the same assumed single-pole, local-Markovian approximation and are not independently derived corneal measurements.

The position-dependent propagator was treated within a local/Wigner approximation, with a quasi-stationary regime assumed for the spectral expressions. We applied this approximation under the assumption that coefficients varied slowly over the relevant wavelength and observation time. Equation (13) yielded a central theoretical prediction of the QFT formulation: the larger the local dissipation rate, the broader the spectral response and the shorter the local correlation time. The Keldysh correlation function G^K contains information about fluctuations or occupation and is determined by the retarded/advanced propagators together with the nonequilibrium noise kernel P^K. The Schwinger–Keldysh formalism therefore describes response and fluctuations simultaneously, and under appropriate conditions the quantum component can be integrated out to obtain a classical stochastic process. To ensure consistency between the Lindblad–Keldysh descriptions, the quadratic noise kernel was treated within a local Gaussian or linearized approximation. Density-type dephasing can produce multiplicative phase noise, whereas linear loss/gain may produce an additive component. Noise normalization and covariance must be derived from the same finite-cutoff Lindblad generator or a specified influence functional; the damping rate alone does not fix the fluctuations.

4. Entropy Production and Information Redistribution

The von Neumann entropy of the total reduced field is

$$S_q = -k_B\,\mathrm{Tr}(\rho \ln \rho). \tag{14}$$

For the present open-field construction, we introduced a spatially resolved Spohn-type relative-entropy relaxation diagnostic; its physical identification with local thermodynamic entropy production requires additional reservoir and coarse-graining information. For local bookkeeping, we defined $\mathscr{L}_x\rho$ as the sum

over dissipative channels c of D[Lc(x)]ρ, and took $\mathscr{L} = \int d^3x\, \mathscr{L}_x$ as the integrated generator. If the dynamical semigroup generated by $\mathscr{L}$ is completely positive and trace preserving and $\mathscr{L}$ admits an appropriate full-rank stationary reference state ρ_{ss} satisfying $\mathscr{L}(\rho_{ss})=0$, a local contribution can be written schematically as follows. The reference state was taken as a faithful stationary state of the integrated dissipative generator. If the full Hamiltonian-plus-dissipative dynamics is used, its stationary-state conditions must instead be imposed consistently. In the elementary finite-cutoff, single-mode linear bosonic loss–gain model, Γloss > Γgain > 0 yields a normalizable, full-support geometric stationary number distribution; when Γgain = 0, the vacuum fixed point is pure, so the unqualified logarithm ln ρss is not faithful on the full Hilbert space. These single-mode conditions are illustrative and do not ensure a faithful invariant state for the complete interacting or spatially coupled field theory, which must be checked separately. The gain rate is unspecified in Table S4; the faithful-state condition is therefore an assumption, not a demonstrated numerical property of the corneal model.

$$\sigma_q(x,t) = -k_{\mathrm{B}}\mathrm{Tr}[(\mathcal{L}_x\rho)\,(\ln\rho - \ln\rho_{\mathrm{ss}})]. \tag{15}$$

Local contributions are not in general pointwise nonnegative; nonnegativity was asserted only for the appropriately defined integrated Spohn functional under its stated assumptions. Equation (15) makes the action of the local dissipative generator explicit as $(\mathscr{L}_x\rho)(\ln\rho - \ln\rho_{ss})$ inside the trace. A suitable support restriction or regularized relative-entropy formulation would be needed if the chosen stationary reference state is not faithful.

$$\Sigma_q(t) = \int d^3x\, \sigma_q(\mathbf{x},t) \geq 0, \tag{16}$$

The time-integrated Spohn-type relaxation is nonnegative if the dynamics is governed by a GKLS generator that preserves the stationary reference state used in the construction [7]. Complete positivity without such a reference state is not sufficient. For time-dependent rates, an instantaneous Spohn functional is nonnegative only when the frozen-time generator admits an appropriate faithful instantaneous stationary state. Time variation of that state adds a reference-state derivative term; monotonicity relative to a time-dependent state does not follow directly. The integrated Spohn functional diagnoses relative-entropy relaxation, not the steady housekeeping entropy-production rate of a driven open system. It vanishes at its reference state even if reservoir currents persist. A larger local damping rate therefore cannot establish a larger physical entropy-production rate without a reservoir-resolved or flux–affinity budget. The strict gain–loss inequality for a full-support single-mode stationary state is stronger than the stability condition Γloss > Γgain and must not be inferred solely from the phenomenological baseline rates.

As a classical transport-side candidate for the independently calibrated physical entropy budget, the local entropy-production density was written schematically using a two-component water–solute description in the barycentric frame, a reduced-heat-flux convention, and a fixed-temperature relative chemical-potential gradient:

$$\sigma_{\mathrm{cl}} = -\frac{1}{T}\mathbf{J}_C^{\mathrm{rel}} \cdot [\nabla(\mu_C - \mu_w)]_T + \mathbf{J}_Q \cdot \nabla\left(\frac{1}{T}\right) + \frac{1}{T}\boldsymbol{\Pi}^{\mathrm{visc}} : \nabla\mathbf{u}. \tag{17}$$

Here J_C^rel is the solute diffusion mass flux measured relative to the barycentric velocity, μ_C and μ_w are specific chemical potentials (energy per unit mass) of solute and water, respectively, J_Q is the reduced heat flux defined consistently with that diffusive reference frame, Π^visc is the deviatoric viscous Cauchy stress (positive dissipative-stress convention), and u is the coarse-grained barycentric fluid velocity. The subscript T specifies the gradient of the relative chemical potential at fixed temperature. With a compatible Newtonian viscous constitutive law, Π^visc:∇u/T contributes nonnegatively to dissipation. Alternative pressure-tensor sign conventions reverse the explicit viscous sign and require a corresponding redefinition of Π. If molar fluxes are employed instead, the chemical potentials and flux normalization must be changed consistently. With consistently defined thermodynamic forces and positive-semidefinite constitutive transport coefficients, the corresponding classical irreversible-thermodynamic entropy production is nonnegative. Equation (17) is a candidate physical contribution, not a measured corneal entropy-production

density; it must be reconciled with reservoir/flux accounting at the chosen coarse-graining scale and must not be added uncorrected to the Spohn-type relaxation diagnostic in Eqs. (15–16). No numerical value of Eq. (17) was calculated in this work.

The matched physical entropy-production rate, defined by a consistent reservoir-resolved or flux–affinity budget, was expressed as

$$\Sigma_{phys,matched}(t) = \int d^3x \left[\sigma_{phys,matched}(\mathbf{x}, t)\right]. \tag{18}$$

The matched physical entropy-production density was defined at a specified coarse-graining scale and must be constructed without double counting classical and quantum descriptions of the same microscopic irreversibility. We kept it distinct from the local Spohn diagnostic. The matched physical entropy budget was defined operationally rather than derived from the uncalibrated Lindblad model. Evaluating it requires identified heat and matter currents, reservoirs or thermodynamic forces, and documented overlap matching. The Spohn inequality alone neither establishes cross-scale additivity nor guarantees positivity of arbitrary local partitions. Local decoherence was interpreted as redistribution of accessible information into the environment and system–environment correlations, rather than fundamental information destruction [17, 19]. A reduced-system entropy increase therefore need not imply loss of information from a larger closed system. Ptaszyński and Esposito [17] provide a theoretical decomposition of entropy production into system–environment correlations and bath deviations, with a further distinction between classically accessible and discord-like correlations.

5. Marangoni-like Coupling and Transport Closure

We introduced a phenomenological free energy per unit area for an effective stromal layer, depending on solute concentration, temperature, structural order, mean field occupation, and connected fluctuations. The stress ansatz was not derived uniquely from the effective Hamiltonian in Eqs. (3–4).

$$\gamma_{\text{eff}} = \gamma_0 + \alpha_C(C - C_0) + \alpha_T(T - T_0) + \alpha_\chi \chi + \alpha_n \langle \hat{n} \rangle + \alpha_G \, C_{2,a}. \tag{19}$$

where

$$C_{2,a}(x, t) = \langle \delta\hat{n}_a(x, t) \, \delta\hat{n}_a(x, t) \rangle. \tag{20}$$

Density and connected-fluctuation observables were interpreted after finite-cell coarse-graining. Explicitly, let $\hat{n}a(x,t) = a^{-3} \int_{\text{cell}(x,a)} d^3x' \, \hat{n}(x',t)$ denote the density operator averaged over a finite cell of volume a^3, and $\delta\hat{n}a = \hat{n}a - \langle \hat{n}a \rangle$. Then C2,a in Eq. (20) is the equal-position connected variance $\langle (\delta\hat{n}a)^2 \rangle$. This cell average is a regularized coarse-grained observable, not an additional microscopic field. The connected-fluctuation measure may more generally be replaced by a nonlocal correlation function. We defined the associated effective tangential stress proxy as follows:

$$\boldsymbol{\tau}_M = \nabla_s \gamma_{eff}, \tag{21}$$

Here ∇_s denotes the gradient projected along the relevant effective interface or stromal layer. In a complete three-dimensional model, this proposed stress proxy would need to enter a hydrodynamic boundary condition or constitutive equation. In the present conceptual model, it was used as a proxy for the hypothesized conversion of thermodynamic and field-theoretic gradients into organized transport, analogous to general Marangoni-flow theory and experiments in related systems [20–23]. For dimensional consistency, the effective layer free energy is per unit area (J m^{-2} = N m^{-1}), and its tangential gradient has units of traction (Pa). If constructed instead from a volume free-energy density, an explicit integration across layer thickness is required. Each coupling coefficient must have compatible units. The corneal stroma lacks a conventional free liquid surface. Accordingly, the proposed stress and transport are termed "Marangoni-like," not classical Marangoni flow or an experimentally established stromal vortex. The proxy requires a separately specified constitutive stress–mobility relation, collagen/poroelastic resistance, fluid

conservation, and boundary conditions before it can predict actual transport. A depth-only Gaussian kernel cannot by itself generate a tangential gradient; lateral heterogeneity or a justified three-dimensional geometry would be needed. The solutal term was assumed to dominate thermal driving as a phenomenological constraint inherited from the previous HEZ models [4, 5], not as an experimentally established property of the corneal stroma. References [20–23] provide evidence and theory for solutal Marangoni effects in other interfacial systems.

6. Correlation Observables and Numerical Procedures

The field formulation retained the first-order equal-time correlation function:

$$G^{(1)}(\mathbf{x}, \mathbf{x}', t) = \langle \widehat{\Psi}^{\dagger}(\mathbf{x}, t)\widehat{\Psi}(\mathbf{x}', t)\rangle, \tag{22}$$

To complement the first-order field correlation, we also defined an equal-time connected density correlation between two coarse-grained spatial locations:

$$C_{nn}^{(c)}(\mathbf{x}, \mathbf{x}', t) = \langle \hat{n}(\mathbf{x}, t)\hat{n}(\mathbf{x}', t)\rangle_c. \tag{23}$$

The connected expectation value in Eq. (23) means $\langle \hat{n}(x,t)\hat{n}(x',t)\rangle - \langle \hat{n}(x,t)\rangle\langle \hat{n}(x',t)\rangle$, with density observables evaluated at the finite coarse-graining scale. This observable can characterize spatially separated density fluctuations but does not by itself establish quantum discord, causal transport coupling, or long-lived correlation memory. Neither this two-point density correlation nor a corresponding correlation length was evaluated numerically or measured in corneal tissue here.

Equation (22) defines a first-order equal-time spatial correlation. The temporal decay time used in Eq. (24) instead refers to the two-time function $G^{(1)}(x; t, t') = \langle \Psi^{\dagger}(x,t)\, \Psi(x,t')\rangle$. For a stationary linear local-Markovian mode, with the corresponding regression assumptions, its first-order amplitude correlation decays proportionally to $\exp[-\Gamma_{\mathrm{eff}}(x)|t - t'|/2]$. This extra dynamical assumption, not the equal-time definition alone, gives $\tau_\Psi \simeq 2/\Gamma_{\mathrm{eff}}(x)$.

For a locally damped diffusive amplitude mode, we adopted the following phenomenological scaling relations:

$$\tau_\Psi(\mathbf{x}) \simeq 2\Gamma_{eff}^{-1}(\mathbf{x}), \qquad \xi_\Psi(\mathbf{x}) \propto \sqrt{D_\Psi/\Gamma_{eff}(\mathbf{x})}, \tag{24}$$

The first-order field-amplitude decay time was distinguished from density relaxation. The correlation-time scaling followed the minimal retarded damping term; the correlation-length scaling additionally assumed overdamped diffusive spatial dynamics. We treated density relaxation as dependent on the loss–gain difference and distinguished its rate from the first-order decoherence rate. The effective diffusion coefficient D_Ψ is a phenomenological parameter of an overdamped, long-wavelength amplitude closure and was not derived from the Schrödinger-type conservative dispersion $\hbar^2k^2/(2m_{\mathrm{eff}})$ in Eq. (3). In particular, $D_\Psi = \hbar/(2m_{\mathrm{eff}})$ is not imposed as a general identity. The displayed length relation requires a diffusive pole or equivalent dynamical reduction; absent this closure, the correlation length must be extracted from a separately specified spatial response or correlation kernel. Neither D_Ψ nor ξ_Ψ was numerically calibrated in this study. The spectral function was defined as follows:

$$\mathcal{A}_\Psi(k, \omega; x) = -2\,\mathrm{Im}\, G^R(k, \omega; x). \tag{25}$$

The spectral function in Eq. (25) was predicted to broaden in regions where Γ_{eff} is large. This is a general consequence of an open-field propagator and was adopted as a new observable that was absent from the original two-level formulation. These analytical relations provided the basis for the depth-dependent numerical calculation reported in Figure 3. For this calculation, we evaluated the dimensionless profiles $\Gamma_{\mathrm{eff}}(x)/\Gamma_{\mathrm{bg}} = 1 + \varphi_{\mathrm{HEZ}}(x)$ and $\tau_\Psi(x)/\tau_{\mathrm{bg}} = [1 + \varphi_{\mathrm{HEZ}}(x)]^{-1}$ over the same depth interval, where Γ_{bg} and τ_{bg} denote their respective reference baselines and $\varphi_{\mathrm{HEZ}}(x)$ is the imposed kernel in Eq. (1).

The modulation amplitude was set to unity as an illustrative input, not estimated from corneal observations. The plotted values were calculated outputs of these prescribed relations.

We evaluated $\varphi(x; x_0, \sigma) = \exp[-(x - x_0)^2/(2\sigma^2)]$ and the normalized local-Markovian relations $r(x) = \Gamma\text{eff}(x)/\Gamma\text{bg} = 1 + \varphi(x)$ and $\tau\Psi(x)/\tau\text{bg} = 1/r(x)$. The prescribed baseline used $x_0 = 70$ μm and $\sigma = 40$ μm across the same 0–450 μm stromal-depth interval. For Table 3, we extracted r, $\tau\Psi/\tau\text{bg}$, and φ at seven specified depths (0, 30, 50, 70, 100, 150, and 200 μm), rounding only the displayed values to three decimals. For Figure 4, we evaluated an illustrative unit-area Lorentzian $A(u; r) = r/[\pi(u^2 + r^2)]$, with $u = 2(\omega - \omega_0)/\Gamma\text{bg}$, using $r = 1$ for a nominal background reference and $r = 2$ at the imposed kernel maximum. Γbg denotes the baseline FWHM in angular-frequency units, so its HWHM is Γbg/2; ω_0 was held constant, and the FWHM of the plotted Lorentzian is 2r in the dimensionless u coordinate (equivalently, FWHM in angular frequency is rΓbg). For Figure 5, we calculated normalized linewidth profiles over 0–450 μm, varying the imposed kernel center x_0 across 50, 70, and 90 μm at fixed $\sigma = 40$ μm, and varying σ across 30, 40, and 50 μm at fixed $x_0 = 70$ μm. The anterior 0–225 μm interval was displayed to resolve the changes. These deterministic calculations were illustrative sensitivity analyses of chosen inputs. The symbol A(u; r) denotes the unit-area illustrative Lorentzian and is not the field spectral function $A\Psi(k, \omega; x)$ of Eq. (25), although both illustrate the same linewidth convention.

7. Entropy-Normalized Transport Efficiency

The Endothelial/HEZ Transport Index (EHTI) was generalized as follows.

$$\mathrm{EHTI}_{\mathrm{QFT}} = \frac{\mathcal{J}_{\mathrm{useful}}}{V_{\mathrm{HEZ}}^{-1} \int_{V_{\mathrm{HEZ}}} d^3x \left[\sigma_{phys,matched}(\mathbf{x})\right]}. \tag{26}$$

The EHTI was defined as a prespecified useful water or solute flux divided by a volume-averaged, independently calibrated physical entropy-production density. Its denominator used the matched physical budget, not an uncorrected sum of classical and Spohn terms. Units are set by the selected flux and are not generally dimensionless. The flux definition, area, volume, averaging interval, sign convention, and coarse-graining prescription must be the same across comparison conditions. A strictly positive, resolvable denominator is required. The EHTI remained prospective; no numerical QFT transport efficiency or improvement was computed.

For a future geometry-independent assessment of candidate localization, we additionally defined a location-dependent transport-to-entropy-cost gain functional:

$$G(x_0) = \frac{\mathcal{J}_{\mathrm{useful}}(x_0)}{V_{\mathrm{HEZ}}^{-1} \int_{V_{\mathrm{HEZ}}} d^3\mathbf{r}\, \sigma_{\mathrm{phys,matched}}(\mathbf{r}; x_0)}. \tag{27}$$

In Eq. (27), x_0 is a freely varied candidate localization parameter rather than an independently measured HEZ depth. The numerator $\mathcal{J}$_useful(x_0) must denote the same prespecified useful flux as the EHTI in Eq. (26); its physical units, sign convention, averaging interval, and evaluation area must remain consistent across candidate positions. The denominator uses the matched physical entropy-production density and must be strictly positive and independently calibrated for each candidate configuration. The candidate volume must be held fixed or adjusted by a consistently specified geometric rule. Maximizing this functional would be a future inverse/optimization test, not a result of the present imposed Gaussian benchmark; neither the flux nor the gain functional was computed here. In the three-dimensional version of Eq. (27), r is the spatial integration coordinate, x_0 denotes the varied localization parameter, and $\sigma_{\mathrm{phys,matched}}(r; x_0)$ is the corresponding matched physical entropy-production density; the volume integral must be evaluated using the same dimensional measure and defined candidate geometry across comparisons. The symbol $\mathcal{J}$_useful denotes a scalar integrated useful flux and is distinct from the local flux vector J_C^rel.

8. Matched-Integrated-Excess-Damping Spatial Control

We performed an additional deterministic control to distinguish the spatial distribution of damping enhancement from its depth-integrated magnitude. Across a prescribed stromal slab $0 \le x \le L = 450\ \mu m$, we defined three nonnegative dimensionless modulation kernels: an anterior Gaussian $\varphi A(x) = \exp[-(x - 70\ \mu m)^2/(2 \times (40\ \mu m)^2)]$, a mirrored posterior Gaussian $\varphi P(x) = \exp[-(x - 380\ \mu m)^2/(2 \times (40\ \mu m)^2)]$, and a uniform kernel $\varphi U(x) = IA/L$, where $IA = \int_0^L \varphi A(x)\, dx$. Because the anterior and posterior Gaussians were mirror images on the same interval, they had the same integral, $IP = IA$; the uniform kernel was normalized to this common area. Thus $\int_0^L \varphi i(x)\, dx = IA$ in all three cases, without assuming that physical entropy-production rates or biological transport were equal. We used the same prescribed local-Markovian response mapping as in Figure 3: $ri(x) = \Gamma eff,i(x)/\Gamma bg = 1 + \varphi i(x)$, and $\tau\Psi,i(x)/\tau bg = 1/ri(x)$. We evaluated the functions at 0.01-μm intervals over 0–450 μm and calculated the anterior-share statistic $Fi(0–150\ \mu m) = [\int_0^{150} \varphi i(x)\, dx]/[\int_0^L \varphi i(x)\, dx]$ using trapezoidal integration. The control held the spatially integrated excess of normalized linewidth, $\int_0^L [ri(x) - 1]\, dx$, fixed; it did not hold reservoir-resolved thermodynamic dissipation fixed. No observed corneal spectrum, fitted HEZ location, independent optimization, full quantum-field evolution, or fluid-dynamical calculation entered this comparison. The reported definitions and grid settings specified a reproducible procedure for Figure 6.

Results

The spatial effective-field construction provided a position-dependent dissipative generator, response/noise observables, and a relative-entropy relaxation diagnostic while retaining solute-dominant driving and possible thermal stabilization as model constraints. Its conditional numerical outputs were the imposed reference kernel (Figure 2), its derived linewidth/correlation-time profiles (Figure 3; Table 3), and the Lorentzian, geometry-sensitivity, and matched-damping controls (Figures 4–6). The proposed EHTI and quantum-to-classical reduction remained prospective; no physical entropy-production budget, transport enhancement, or DDS function was computed. The additional classical transport entropy expression, connected density-correlation observable, and candidate-position gain functional were proposed definitions only; none was evaluated with independent experimental data or added to the deterministic numerical outputs.

1. Method–Result Correspondence and Scope

The distinction between theoretical definitions and numerical findings was maintained throughout. Figure 2 visualized a prescribed Gaussian input; Figure 3 and Figures 4–6 displayed deterministic responses to chosen local-Markovian mappings. Their calculated values did not result from fitted corneal measurements or full quantum-field evolution. The microscopic field identity, field–matter coefficients, absolute Marangoni-like stress, and physical transport efficiency remained uncalibrated. Thus, the calculations yielded benchmark signatures and controlled spatial comparisons for future tests, not independent evidence for HEZ localization.

2. The HEZ Was Represented as a Localized Dissipative-Field Kernel

The most immediate consequence of the reformulation was a change in the mathematical status of the HEZ. In the finite-dimensional model, a quantum subsystem was placed within a prescribed HEZ profile. In the field theory, the HEZ was encoded in the spatial coefficients of the generator itself. Local effective damping, noise, field potential, and entropy-production density were permitted to depend on $\phi_{\mathrm{HEZ}}(x)$. The HEZ was therefore identified in the proposed model as a region in which the open-field action contained an enhanced dissipative contribution.

Schematically, this was written as follows.

$$\Gamma_{\mathrm{eff}}(x) = \Gamma_{\mathrm{bg}} + \Delta\Gamma\,\phi_{\mathrm{HEZ}}(x) + \Gamma_{\mathrm{sol}}(x) + \Gamma_{\mathrm{T}}(x), \tag{28}$$

The decomposition in Eq. (28) was obtained from Eqs. (10) and (11) under the assumption that the three local channel rates shared the displayed localization kernel and gradient-response functions: $\Gamma bg = \Gamma loss,0 - \Gamma gain,0 + \Gamma\varphi,0$; $\Delta\Gamma = \lambda loss^{H} - \lambda gain^{H} + \lambda\varphi^{H}$; $\Gamma sol = (\lambda loss^{c} - \lambda gain^{c} + \lambda\varphi^{c})\,FC[\nabla C]$; and $\Gamma T = (\lambda loss^{T} - \lambda gain^{T} + \lambda\varphi^{T})\,FT[\nabla T]$. These were defined as signed composite coefficients: the nonnegativity of each individual Lindblad rate does not require each composite solutal or thermal contribution to be positive. The numerical reference calculations held the other contributions fixed or incorporated them into Γbg and prescribed $\Delta\Gamma/\Gamma bg = 1$, producing $\Gamma eff/\Gamma bg = 1 + \varphi HEZ(x)$. Here Γsol denotes the composite solute-dependent linewidth contribution, whereas the subscript c in Eq. (10) labels a dissipative channel (dephasing, loss, or gain); these are different quantities.

Here Γ_{bg} represented background damping, and the remaining terms represented HEZ, solutal, and thermal contributions. In Keldysh language, the same spatial profile also appeared in the imaginary/noise part of the effective action. The term “High Entropy-Production Zone” thereby acquired a field-theoretic definition: a hypothesized region of heightened physical entropy production represented by spatially modified open-field coefficients. The implemented kernel was specified to enhance modeled local relaxation, but stronger relaxation alone did not establish a higher thermodynamic entropy-production rate; independent flux and reservoir accounting was required. In numerical implementation, $x_0 = 70$ μm, σ =

40 μm, and 50–100 μm were retained as reference values for comparison. The HEZ itself, however, was defined as a quasi-two-dimensional dissipative field with a maximum immediately beneath Bowman's layer and continuous axial and radial decay. Accordingly, the theory was not interpreted as an independent QFT prediction of 70 μm or 40 μm. In the Figure 2 numerical profile simulation, we obtained the prescribed Gaussian maximum at 70 μm and the imposed decay with the characteristic width of 40 μm. This simulation evaluated only the assumed spatial profile; it did not provide a first-principles prediction or an inverse reconstruction of the HEZ location or its physical entropy-production rate.

3. Solute-Dominant Driving Was Preserved as a Model Constraint

In the original model, the effective solutal contribution to Marangoni-like driving exceeded the thermal contribution. To preserve this result in the field formulation, the solute-sensitive terms contained in γ_{eff}, U_{eff}, and/or Γ_c were required to exceed the corresponding temperature-sensitive terms under the reference conditions. This hierarchy remained a phenomenological condition inherited from the original model and would become testable only if the coefficients were measured independently. In the field theory, solutal effects were decomposed into contributions to the mean effective potential, local damping, field occupation, and connected fluctuations. The decomposition was therefore considered capable of distinguishing in future work whether solute dominance was energetic, dissipative, or fluctuation mediated. The field-corrected free-energy formulation thus provided an explicit theoretical route by which local field occupation and connected fluctuations could modify the effective Marangoni-like stress proxy. In this context Γc labels the channel-resolved rates of Eq. (10), not the composite solutal linewidth Γsol of Eq. (28).

4. Thermal Stabilization Was Represented as a Dissipation–Noise Channel

Temperature coupling was represented not as the primary driving force but as a channel that could stabilize fluctuations through both retarded damping and Keldysh noise. Even when its contribution to the mean Marangoni-like driving was small, enhanced damping could suppress unstable fluctuations. The thermal channel was allowed to increase Γ_{eff}, thereby suppressing long-lived fluctuations while its contribution to mean Marangoni-like driving remained smaller than the solutal term. This gave thermal stabilization a field-theoretic meaning: even if the thermal channel was not the main source of directional transport, it could reduce the lifetime and amplitude of field fluctuations. Conversely, if thermal noise increased faster than damping, fluctuations could instead be amplified. The theoretical analysis indicated that quantitative prediction would require constraints from a fluctuation–dissipation relation or a nonequilibrium noise model; no quantitative thermal-stabilization simulation was performed.

5. Sub-Bowman Localization Was Explicitly Distinguished from the Simulation Reference Geometry

The 70/40 μm and 50–100 μm values were retained as reference geometry, whereas conceptual HEZ localization was defined not by a fixed depth but by a maximum immediately beneath Bowman's layer followed by continuous decay toward the endothelium and the periphery. This distinction was important. A genuine first-principles prediction of the preferred depth would have required deriving the spatial dependence of g_χ, g_C, and g_T, together with the collagen-order potential, transport coefficients, boundary conditions, and local dissipation rates, from corneal microstructure and physiology. Such data were not included in the present baseline model. The resulting field-theoretic statement was therefore that HEZ localization was compatible with and built into the QFT, but was not independently proven by it. It remained possible for a future independently constrained model to test whether an anterior optimal depth emerged from transport-to-dissipation efficiency rather than an imposed Gaussian profile. Equation (27) was introduced to formalize a possible future comparison of candidate depths using useful flux relative to an independently calibrated entropy-production cost; no optimal location was selected in the present study.

6. A Spatially Resolved Entropy-Relaxation Diagnostic Was Defined

Whereas the two-level model produced a single quantum-entropy trajectory, the field theory introduced a spatially resolved relative-entropy diagnostic $\sigma_q(\mathbf{x}, t)$. Even if the spatial integral changed monotonically, transport and intermode coupling could redistribute entropy production, so local regions could display distinct transient behavior. Relative to a comparable HEZ-off model in which ϕ_{HEZ} and its associated dissipative coupling were removed, the HEZ hypothesis postulated an enhanced physical entropy-production contribution in the anterior region, but the prescribed dissipative kernel did not prove this consequence. Importantly, a large σ_q did not necessarily imply efficient transport. Because efficiency depended on the ratio of organized flux to dissipative cost, $\mathrm{EHTI}_{\mathrm{QFT}}$ remained necessary. This spatial formulation clarified that microscopic decoherence and macroscopic convection were not identical phenomena but processes on different scales linked through effective stress and coarse-graining. The result obtained here was the definition of a spatially resolved relative-entropy relaxation diagnostic, not a derived numerical elevation of steady-state entropy production in the HEZ. Separating Spohn relaxation from environmental entropy flow and estimating the latter using independently calibrated fluxes and affinities were identified as necessary before the adjective "high entropy-production" could be confirmed thermodynamically. Equation (18) defined the required matched physical entropy budget; that budget could not be evaluated numerically from the uncalibrated σcl and Spohn σq terms alone. The separate classical transport expression in Eq. (17) was introduced as a possible flux–force contribution to such a physical budget, not as an independent quantum correction or a justification for adding the classical and Spohn terms.

7. Spectral Broadening and Shorter Correlation Times: Analytical and Numerical Results

The assumed local-Markovian field propagator yielded a conditional, testable spectral signature. In the Markov limit, $\Gamma_{eff}(x)$ entered the imaginary part of the inverse retarded propagator. Therefore, in regions with enhanced local damping, the collective field represented by Ψ was predicted to exhibit a broader spectral response and a shorter correlation time.

For a simple Lorentzian mode,

$$A(\omega; x) \propto \frac{\Gamma_{eff}(x)}{[\omega - \omega_0(x)]^2 + [\Gamma_{eff}(x)/2]^2}. \tag{29}$$

In Eq. (29), frequency is an angular frequency, Γeff(x)/2 is the Lorentzian HWHM, and FWHMω(x) = Γeff(x). The unit-area curves in Figure 4 were instead plotted against u = 2(ω − ω₀)/Γbg, where Γbg is the background angular-frequency FWHM, so the dimensionless Lorentzian has HWHMu = r and FWHMu = 2r. This change of horizontal coordinate does not alter either the twofold linewidth ratio or the one-half peak-height ratio.

For Eq. (29), the full width at half maximum was shown to be proportional to Γ_{eff}. This derivation did not specify which experimental spectroscopic method could access the relevant field. It did, however, convert the HEZ hypothesis into a measurable spatial signature. If an experimentally observable collective hydration/proton mode can be identified, its relaxation or linewidth should vary systematically with stromal depth and correlate with the proposed HEZ profile. Likewise, if long-wavelength fluctuations are diffusive, $\xi_\Psi \propto \sqrt{D_\Psi/\Gamma_{\mathrm{eff}}}$ predicted a shorter correlation length in the most strongly damped region of the HEZ. Conversely, an increased correlation length would suggest that ordering interactions or driven collective behavior dominate over simple damping. Both possibilities were regarded as potential constraints on the theory. As an indirect experimental precedent connecting dissipation of collective vibrational modes to observables, Caprini et al. estimated heat absorption and entropy production of laser-excited phonons from time-resolved X-ray scattering [24]. Although that result concerned a crystalline system and did not directly support the cornea, it provided a relevant validation precedent for combining time-resolved spectroscopy with measurements of dissipation, occupation, and relaxation. The Figure 3 numerical calculation yielded

a maximum normalized spectral linewidth of 2.0 and a minimum normalized first-order field-amplitude correlation time of 0.5 at the imposed 70-μm reference center, compared with their respective unit background values. Across the prescribed depth profile, linewidth increased as local damping increased, whereas the first-order correlation time decreased reciprocally. This paired spatial response constituted an illustrative, model-derived numerical result; the extrema and their location followed from the selected unit modulation and imposed Gaussian reference geometry, rather than independent prediction or corneal measurement. The length scaling in Eq. (24) presumes an overdamped diffusive mode; it is not a direct consequence of Eq. (3) alone.

The numerical extraction of the prescribed Gaussian profile gave $\varphi = 1.000$, $\Gamma\text{eff}/\Gamma\text{bg} = 2.000$, and $\tau\Psi/\tau\text{bg} = 0.500$ at the assumed 70 μm center, compared with approximately unity for the normalized linewidth and correlation time at large distances from the center (Table 3). At 50 μm, the corresponding quantities were 0.882, 1.882, and 0.531, respectively; at 100 μm, they were 0.755, 1.755, and 0.570. These numbers were generated directly from the imposed equations rather than estimated from corneal observations. The unit-area Lorentzian illustration (Figure 4) produced a twofold full-width-at-half-maximum ratio and a one-half peak-height ratio for $r = 2$ versus $r = 1$, while conserving integrated spectral area by construction. In the geometry sensitivity sweep (Figure 5), moving x_0 from 50 to 90 μm translated the normalized linewidth maximum to the corresponding imposed positions without altering its height of 2.000; changing σ from 30 to 50 μm at fixed $x_0 = 70$ μm broadened the Gaussian-excess full width at half maximum from 70.6 to 117.7 μm, also without changing the central height. Thus, the center and spatial extent of the illustrated signal tracked the assumed reference geometry.

8. Information Dissipation Was Represented as Redistribution into Environmental Correlations

The open-system interpretation allowed reduced local phase information to become inaccessible while information persisted in environmental states and correlations. This was a theoretical information-redistribution account, not a demonstration of corneal quantum decoherence or an increase in physical entropy production.

9. The EHTI Was Retained as a Field-Theoretic Efficiency Index

The original EHTI compared useful flux with entropy-production density. The field-theoretic index preserved this concept while adding spatial and channel resolution. If the HEZ-induced increase in organized flux exceeded the increase in the denominator, EHTI_{QFT} was expected to rise; if dissipation increased without improving transport, the index was expected to fall. A functional dissipative structure was therefore evaluated conceptually not only by the magnitude of entropy production but also by its ratio to useful organized transport. The model therefore did not assume that “more decoherence is more beneficial.” Because the new QFT couplings were uncalibrated, the EHTI improvement reported in the prior model was not reasserted here as an independent result; the principal result was instead that the efficiency concept could be defined consistently within the field theory. The efficiency statement was conditional on an operationally fixed numerator and a positive, independently calibrated dissipative denominator. No numerical EHTI ratio, field-corrected stress, or HEZ transport improvement was computed in the present QFT reformulation. A finite steady-state EHTI could not be established using the vanishing Spohn relaxation functional alone; a physical entropy-flow budget was required. The candidate-location gain functional in Eq. (27) was proposed to extend this idea to an adjustable spatial parameter, but neither a flux-based gain maximum nor a preferred depth was calculated.

10. A Formal Reduction Pathway to the Classical Limit Was Outlined

In a strong-decoherence, long-wavelength regime, a classical stochastic description could be obtained by a controlled elimination of fast physical modes and a suitable treatment of the Keldysh response field, as in Keldysh treatments of driven open quantum systems [12]. The elimination was not evaluated explicitly for

measured stromal coefficients. Related field-theoretic coarse-graining of reaction–diffusion systems provided a useful basis for classical comparison [25]. Schematically,

$$\partial_t \Psi_{\mathrm{cl}} = -\frac{i}{\hbar}\frac{\delta F_{\mathrm{eff}}}{\delta \Psi^*_{\mathrm{cl}}} - \frac{\Gamma_{\mathrm{eff}}}{2}\Psi_{\mathrm{cl}} + \eta. \tag{30}$$

Here F_eff denoted the coarse-grained effective free-energy functional associated with the conservative sector, and η denoted a zero-mean stochastic field whose correlation function was determined by the Keldysh noise kernel. This functional was a phenomenological coarse-grained energy functional; its identification and the exact drift coefficient had to follow from a specified reduction, rather than from decoherence alone. The noise correlator associated with Eq. (30) was determined by the Keldysh kernel and was therefore left general in the driven nonequilibrium HEZ. Only in an equilibrium or near-equilibrium specialization would it have been appropriate to reduce it to a fluctuation-dissipation form proportional to temperature and a kinetic coefficient.

Scope of the stochastic reduction. In particular, the additive-noise notation η in Eq. (30) was a schematic Gaussian approximation. With the density-dephasing channel of Eq. (7), a more faithful stochastic reduction was expected to admit a multiplicative phase-noise term and could include nonlocal or colored correlations after integrating out fast variables. The effective stochastic calculus, noise normalization, and any Itô/Stratonovich correction had to be specified for quantitative simulation. The Keldysh quantum field served as a response/integration variable in this construction; it was not itself identified with a separate physical field whose rapid decay justifies the classical limit. Reduction to Eq. (30) required an explicitly stated linearization and noise approximation.

The Keldysh sector determined noise correlations; with further coarse-graining, the theory could be connected to diffusion–advection or hydrodynamic equations for density-like variables. Quantum–classical consistency here did not mean that Gibbs entropy and von Neumann entropy are identical. What was regarded as consistent was the direction of irreversibility after coarse-graining, the localization of dissipation, and the hierarchy of transport responses. The classical advection–diffusion representations inherited from the previous model were therefore interpreted as a coarse-grained transport limit rather than independently simulated results. The pathway in Eq. (30) was presented as a consistency proposal at the level of a formal coarse-grained effective equation. It did not constitute a controlled numerical integration of the corneal Hamiltonian and dissipators or a derivation of the fluid velocity, pressure, collagen poroelastic response, or Marangoni-like flow. Establishing such a reduction would have required identifying the retained slow variables, evaluating the corresponding Keldysh noise and dissipative kernels, imposing the conservation and boundary equations, and demonstrating that the resulting classical transport coefficients reproduce measured corneal responses. In particular, the conserved water/solute variables and their fluxes would have to be retained or reconstructed explicitly; rapid damping of the field amplitude alone did not determine Darcy flow, transverse advection, or a stromal vortex.

11. Matched-Damping Controls Separated Spatial Profiles but Did Not Identify the HEZ

The three prescribed kernels had a common integrated excess of normalized damping, IA = IP = IU = 96.249 μm (mean uniform modulation IA/L = 0.213886). Nevertheless, their spatial responses differed markedly (Figure 6). For the anterior Gaussian, 97.63% of the excess damping lay in the anterior 0–150 μm region, compared with 33.33% for the uniform control and less than 0.001% for the mirrored posterior Gaussian. At the imposed 70-μm anterior reference center, the calculated normalized linewidths were 2.000, 1.214, and approximately 1.000, respectively; the corresponding normalized first-order correlation times were 0.500, 0.824, and approximately 1.000. The posterior Gaussian instead reached a linewidth of 2.000 and a correlation-time ratio of 0.500 at its imposed 380-μm center. These outputs demonstrated only that the simple damping-to-linewidth and reciprocal-correlation-time mapping retained the imposed positional information even when the total integrated excess damping was matched. They did not show that anterior localization was selected by the field equations, that the HEZ existed, or that thermodynamic entropy

production, stromal stress, and transport had been independently calculated. Actual depth localization would have to be inferred from measurements or an independently constrained inverse analysis without prescribing any of these three kernels.

Discussion

The principal contribution of this study was the extension of the HEZ from a localized two-level open system to a spatially distributed open nonequilibrium effective quantum field. This extension allowed dissipation, noise, response, correlations, information redistribution, free-energy gradients, and transport to be represented within an integrated, position-dependent theoretical description. However, the present study did not demonstrate the existence of the HEZ, the empirical validity of the 70/40 μm values, long-lived macroscopic quantum coherence, or the necessity of discord-like correlations or correlation memory. Its role was not to elevate the HEZ to an experimentally established fact, but to organize it as a theory testable by depth-resolved spectroscopy, correlation measurements, transport measurements, and inverse-problem analysis. The two-level model was suitable for describing local decoherence and entropy production, but was insufficient for treating correlations across tens to hundreds of micrometers, spectral responses, or coupling between localized microscopic processes and macroscopic gradients. In the field theory developed here, the HEZ was represented as a position-dependent modification of the effective Hamiltonian and dissipative generator, which allowed response and noise to be described in the same spatial region. At the same time, interpreting the theory as an effective field prevented overstatement: the field Ψ was not claimed to be a macroscopic corneal wavefunction, but a mathematical representation of coarse-grained collective modes. Such a field variable was considered meaningful even when coherence times were short because response and correlation functions could be defined and measured even in strongly dissipative systems. The principal new quantities introduced were G^R, G^A, and G^K. The retarded and advanced functions were used to describe response, while the Keldysh function was used to describe occupation and fluctuations. The analysis recognized that these functions were linked at equilibrium by the fluctuation–dissipation theorem, whereas a driven biological tissue was not required to satisfy that equilibrium relation; departures from it were considered potential measures of nonequilibrium behavior. The HEZ was therefore framed as testable not only through proposed elevation of entropy production but also through possible differences in noise–response relations relative to surrounding tissue. Future simultaneous measurements of spontaneous fluctuations and externally driven responses may provide a more discriminating evaluation of local nonequilibrium behavior. The classical, finite-dimensional quantum, and open quantum-field versions of the HEZ model were compared in Table 2.

Figure 3 was best interpreted as a conditional numerical result of the open-field formulation rather than solely as a schematic description of the calculation. With the Gaussian HEZ reference profile prescribed in advance, the minimal local-Markovian relations generated an increase in normalized spectral linewidth and a reciprocal decrease in first-order field-amplitude correlation time. At the assumed 70-μm center, their normalized values were 2.0 and 0.5, respectively. This correspondence was a consequence of the chosen damping dependence; it neither independently identified an anterior HEZ nor established greater physical entropy production, organized Marangoni-like transport, DDS function, or correlation memory. Nevertheless, the paired observables supplied a testable prediction of the specified model: independent depth-resolved measurements of an identified collective mode should assess whether linewidth broadening co-localizes with shorter first-order correlations. Deviations from the reciprocal Markovian relation could motivate examination of frequency-dependent damping, structured noise, interactions, or non-Markovian effects, but they would not alone establish any specific alternative. Experimental parameter estimation and spatial reconstruction should be performed without imposing the 70/40-μm reference geometry.

The hypothetical concept of a “Dissipative Decoherence Structure” was clarified by the field theory in a way that distinguished yet connected microscopic decoherence and macroscopic dissipative structure. A dissipative structure was understood to maintain macroscopic order through free-energy consumption and fluxes, whereas decoherence was defined as loss of phase relations in a reduced quantum state through environmental coupling. They were distinguished as different descriptive levels but could be connected when the same environmental coupling contributed to microscopic relaxation, coarse-grained transport coefficients, noise, and entropy production. The proposed causal chain was therefore: gradients → environmental coupling and microscopic relaxation → coarse-grained free-energy/stress gradients →

organized transport. Thermodynamic entropy production, von Neumann entropy, Shannon information, and quantum mutual information were recognized as related but nonidentical quantities. General theoretical reviews had addressed the relationship between quantum information and thermodynamics [19]. In this theoretical interpretation, an increase in the entropy of the reduced field was interpreted as a reduction in locally accessible quantum information. Because information could be redistributed into environmental states or nonlocal correlations, "information dissipation" was taken to mean a reduction in local accessibility and re-encoding into correlations. Because local information could be redistributed into environmental degrees of freedom and system–environment correlations, separate evaluation of von Neumann entropy, quantum mutual information, and classically accessible correlations was required. For two coarse-grained local field modes A and B representing different stromal positions, or an HEZ mode and an environmental mode, total correlations were defined as evaluable by quantum mutual information. Three mathematical qualifications were identified to delimit this proposal. First, the nonnegative Spohn functional defined in Eqs. (15–16) was used to measure relaxation relative to a specified stationary state; a large dephasing or damping rate did not establish a large steady thermodynamic entropy-production rate. A physically interpretable HEZ dissipation map would instead need reservoir-resolved entropy currents or an independently calibrated flux–affinity construction, with no double counting of coarse-grained classical contributions. Second, the admissibility of the local Lindblad model required nonnegative local channel rates and a stable loss/gain sector; the effective Hamiltonian also had to satisfy boundedness conditions. Third, the link from quantum-field observables to the Marangoni-like stress in Eqs. (19–21) remained a phenomenological constitutive hypothesis, not a first-principles derivation of corneal fluid motion.

The Müller–Schäfer analysis also sharpened an important distinction for the proposed Dissipative Decoherence Structure [18]. Decoherence was described as a possible early entropy-generating stage, distinct from later collisional or thermodynamic equilibration: loss of phase information could raise the entropy of the reduced field even before the system reaches a thermal state. In HEZ terms, the analogy was not taken to imply that corneal collective modes reproduced QCD dynamics; instead, environmental phase randomization was considered a possible contributor to local reduced-state entropy while subsequent coarse-grained transport, mixing, relaxation, and boundary fluxes account for additional classical entropy production. Whether this mechanism was quantitatively important in the cornea remained an experimental question; the high-energy calculation supplied a proof-of-principle for field-mode entropy generation, not evidence for the magnitude or timescale of corneal decoherence. Its more distinctive feature would be a local conversion capacity: decoherence-associated loss of locally accessible phase information and its redistribution into system–environment correlations would be coupled, through coarse-grained free-energy, chemical-potential, hydration, or stress gradients, to useful classical transport. The relevant proposed criterion was therefore conversion efficiency rather than dissipation alone, conceptually consistent with the EHTI, which was designed to assess whether organized flux increases more than its dissipative cost. In this sense, the HEZ would qualify as a DDS only if microscopic information redistribution is spatially organized and functionally linked to macroscopic transport; this remained a testable hypothesis rather than an established property of corneal tissue.

Within this effective-bosonic interpretation, candidate physical realizations of the coarse-grained field include hydration-shell fluctuations, hydrogen-bond vibrations, collective proton-coupled motion, and collagen–water coupled vibrations. The wider collagen–water–proton–hydrogen-bond network may also provide a plausible environment for chiral-phonon-like collective modes because it combines structural chirality, dynamic hydration, proton mobility, and coupled hydrogen-bond vibrations. The mean occupation number $\bar{n}$ was therefore proposed as a potentially useful quantity for linking microscopic collective motion with macroscopic entropy production [18]. If future measurements or microscopic calculations show that dominant HEZ-associated Bose-like or chiral-phonon-like modes have a mean occupation of order unity ($\bar{n} \approx 1$) under physiological temperature and hydration conditions, the HEZ may lie in a regime in which both open-quantum entropy production and classical coarse-grained transport should be considered, rather than assuming that either description is sufficient a priori. This remained a conditional, experimentally testable hypothesis; neither such modes nor an occupation number near unity had been demonstrated in the cornea.

For a single coherent bosonic mode with mean occupation $\bar{n} = |\alpha|^2$, complete decoherence converts the pure coherent state into a diagonal Poisson mixture and generates a decoherence entropy Sdec. In their calculation, Sdec/Seq remained above 0.75 up to $\bar{n} = 10$, while in their color-glass application $\bar{n} \approx 3$ gave a decoherence contribution of order one-half of the eventual equilibrium/final entropy, with a characteristic decoherence time $\tau dec \sim 1/Qs < 0.2$ fm/c.

$$I(A:B) = S(\rho_A) + S(\rho_B) - S(\rho_{AB}) \tag{31}$$

Information-unit convention for Eqs. (31–32). In this section, $S(\rho) \equiv -\mathrm{Tr}[\rho \ln(\rho)]$ was used as the dimensionless von Neumann information entropy, expressed in nats. Accordingly, I(A:B), J(A|B), and D(A|B) were also expressed in nats. The thermodynamic entropy in Eq. (14) was defined as $S_q(\rho) = k_B S(\rho)$, with units J K^{-1}. When comparing information-theoretic correlations with physical entropy budgets, the conversion factor k_B had to be included; neither the mutual information nor the discord-like residual was counted as an additional physical entropy-production rate. Because the mutual information in Eq. (31), I(A:B), included both classically accessible and potentially nonclassical correlations, a nonzero I(A:B) alone did not demonstrate quantum discord [17]. If a Gaussian approximation was physically justified, a two-mode covariance matrix could be constructed from two-point correlation functions. The diagonal blocks represented fluctuations of modes A and B, while the off-diagonal block represented intermode correlations. Although a nonzero off-diagonal block indicated cross-mode covariance, such covariance data alone did not verify the quantum nature of correlations in corneal tissue unless the underlying Gaussian quantum-state description was independently justified. The connected density correlation in Eq. (23) was introduced as a distinct spatial observable alongside first-order field coherence.

A candidate two-mode covariance matrix V was considered physically admissible only if it was real and symmetric and obeyed the bosonic uncertainty relation $V + i\Omega/2 \succeq 0$ for dimensionless canonical quadratures $R = (q_A, p_A, q_B, p_B)$ with $[q_j, p_k] = i\delta_{jk}$. Here $V_{jk} = \langle\{\Delta R_j, \Delta R_k\}\rangle/2$ and Ω denoted the two-mode symplectic matrix $\Omega = Jsp \oplus Jsp$, $Jsp = [[0, 1], [-1, 0]]$. For dimensionful quadratures satisfying $[q_j, p_k] = i\hbar\delta_{jk}$, the corresponding condition was $V + i\hbar\Omega/2 \succeq 0$. Let J(A|B) denote the classically accessible correlation optimized over a clearly specified class of local measurements on B. The residual was then defined schematically as follows. For an optimization over all admissible local positive-operator-valued measurements (POVMs), this corresponded to conventional quantum discord for measurements on B; a restriction to Gaussian measurements instead defined a Gaussian-restricted residual. The two-dimensional symplectic block Jsp is unrelated to the classically accessible correlation J(A|B) and to the transport flux symbols used earlier.

$$D(A \mid B) = I(A:B) - J(A \mid B) \tag{32}$$

The distinction between multipartite and two-mode correlations was essential for applying Ref. [17] to the HEZ. Ptaszyński and Esposito defined classical and quantum contributions for correlations distributed over the full system–environment ensemble; Eq. (32), by contrast, concerned a selected pair of effective field modes A and B. These two partitions could not be treated as numerically or operationally equivalent without an explicit mode decomposition and corresponding measurement protocol. For a fixed bipartite quantum state, let $J_G(A|B)$ be optimized over local Gaussian measurements only, and let $J_{all}(A|B)$ be optimized over all admissible local POVMs on B. Because $J_G(A|B) \leq J_{all}(A|B)$, the Gaussian-restricted residual $D_G(A|B) = I(A:B) - J_G(A|B)$ was an upper bound on the corresponding unrestricted discord $D(A|B) = I(A:B) - J_{all}(A|B)$, provided the same state, bipartition, and measured subsystem are used. This upper-bound relation had to be distinguished from the special mathematical properties of exact Gaussian quantum states. For an exactly Gaussian, physically admissible bipartite state, a nonzero intermode covariance block implied a nonproduct state and nonzero quantum discord, even though the state did not necessarily have to be entangled. By contrast, a positive Gaussian-restricted residual inferred from an approximate covariance model did not, by itself, constitute evidence of quantum discord in an underlying corneal state that might be non-Gaussian: an unrestricted measurement could reveal additional classically accessible information, and discord computed for a Gaussian approximation was not generally a bound on the discord of a different,

non-Gaussian physical state. The Wehrl/heterodyne mutual information discussed in Ref. [17] provided an operationally defined accessible classical-correlation contribution, not generally the unrestricted optimum.

In the present HEZ model, the measurement class, the relevant mode partition, and the microscopic Hilbert space had not been experimentally fixed. The Hilbert space was treated as the abstract state space in which quantum states and operators of the selected effective microscopic degrees of freedom were defined; its detailed realization remained unspecified because the corresponding corneal quasiparticles and measurement basis had not been identified. Accordingly, the residual component in Eq. (32) was described conservatively as a discord-like correlation index within a selected Gaussian effective model, rather than as established quantum discord in biological corneal tissue. In a previous preliminary AI-assisted conceptual virtual analysis conducted in accordance with the methodology described in Reference 17, the G1 condition reported by the author in Reference 4, which combined HEZ, solute-driven Marangoni-like coupling, and thermal Marangoni-like coupling, was represented as a high-temperature bosonic Gaussian system. In that illustrative analysis, most of the modeled correlations were classically accessible, with a non-negligible residual correlation inaccessible to the chosen local Gaussian measurements. That analysis was neither an experimental measurement nor an independently validated simulation, was not part of the present Methods or Results, and was mentioned solely as a motivation for future tests. The bosonic Gaussian analysis in Ref. [17] indicated that classical position–momentum correlations could dominate in an appropriate high-temperature or large-occupation regime, while the balance also depended on the initial state; a quantum contribution was not categorically excluded by a warm environment. Physiological corneal temperature alone did not determine the ratio of relevant mode energies to k_B T or the occupation statistics of putative hydration/proton excitations. Nor was a discord-like component regarded as the direct cause of Marangoni-like flow. More conservatively, thermodynamic gradients could alter environmental coupling and correlation redistribution, while any influence on classical transport would have to be mediated through an independently justified coarse-grained free-energy, chemical-potential, or stress–mobility relation. Discord-like correlations were therefore not treated as a necessary premise of the HEZ hypothesis, but as a possible additional microscopic correlation diagnostic. A zero residual would not falsify the classical HEZ–Marangoni-like hypothesis. Conversely, a reproducible nonzero Gaussian-model residual would require validation of the physical state and mode partition, assessment of non-Gaussian alternatives, and a sufficiently unrestricted classical-correlation optimization before it could be interpreted as evidence of quantum discord in corneal tissue. Within the HEZ, some correlations generated by previous dissipative processes were hypothesized to persist for a finite time and subsequently influence relaxation, gradient formation, transport, or structural order, producing correlation memory. This was not taken to mean biological memory or permanent preservation of a quantum state. Perturbations of hydration, solute concentration, temperature, collagen–water interactions, or proton-related degrees of freedom could redistribute information across spatial, molecular, and system–environment correlations. If these correlations decayed more slowly than the original fast degrees of freedom, they could act as a transient physical record of the preceding state. Conceptually, this was expressed as perturbation → dissipation → information redistribution → transient correlation memory → organized recovery. In field-theoretic terms, this property was expressed schematically by a connected two-time correlation function.

$$\mathcal{C}_{AB}(t,t') = \langle \delta A(t)\, \delta B(t') \rangle_c \tag{33}$$

For operator-valued A and B, Eq. (33) uses the displayed operator ordering. If symmetrized correlations are required, the connected expectation value of the anticommutator of δA(t) and δB(t′), divided by two, should be used instead. The appropriate choice depends on the observables and measurement protocol. A and B were allowed to represent the hydration/proton field, order field, density, stress, or related quantities. When τ_env ≪ τ_sys, the Markovian Lindblad approximation was considered appropriate; however, when the correlation time τ_mem becomes comparable to the system relaxation time, transport time, or gradient-reformation time, history dependence could no longer be ignored.

A possible non-Markovian evolution was illustrated schematically in Eq. (34).

$$\partial_t Q(t) = F[Q(t)] - \int_0^t K\,(t - t')\,Q(t')\,dt' + \xi(t) \tag{34}$$

In Eq. (34), Q(t) is a generic slowly evolving coarse-grained variable and is distinct from the prescribed, time-independent HEZ spatial kernel φHEZ(x) of Eq. (1). The memory kernel K is hypothetical and was not estimated from corneal data.

Within the Schwinger–Keldysh/influence-functional formalism, correlation memory could be represented by temporally nonlocal self-energies, frequency-dependent responses, and colored noise, and could be incorporated as a non-Markovian extension of the existing QFT formulation [10, 26, 27]. In this picture, even if the system approached the same final state, its recovery pathway could depend on the history of previous perturbations. Discord-like correlations and correlation memory were distinguished. A nonzero discord-like component did not automatically imply memory, and correlation memory did not require quantum discord; temporal memory could not be inferred from an equal-time covariance matrix or a single-time mutual-information value. The hypothesis could be tested by examining hysteresis after controlled perturbation, history-dependent recovery, multiple relaxation times, and deviations of two-time correlations from simple Markovian decay. Absence of such signatures was considered consistent with the sufficiency of a local Markovian Lindblad-QFT description. Conversely, reproducible history dependence or a finite-time memory kernel would provide grounds for extending the HEZ to a non-Markovian open field. Consistent with the proposed possibility of correlation memory, Fanchini et al. showed in a solvable two-qubit model that non-Markovian reservoirs can sustain or regenerate quantum discord even when entanglement temporarily vanishes, and that a common reservoir can create discord without entanglement [28]. This result provided a theoretical precedent for environment-mediated correlation dynamics.

Quantum–classical consistency was not taken to mean that classical and quantum entropy curves numerically coincided; rather, after appropriate coarse-graining, both descriptions were expected to connect to the same effective generator. From this perspective, double counting of classical and quantum entropy could be reduced by integrating out quantum fluctuations at a matching scale and transferring their effects into renormalized classical transport coefficients. Concentration gradients can alter interfacial tension and generate Marangoni flow in other systems [20–23]. The QFT reformulation did not make this assumption more empirically established, but its decomposition of solutal effects into multiple pathways—mean free energy, local damping, field occupation, and fluctuation corrections—created a route for distinguishing them experimentally. Within the adopted phenomenological description, thermal stabilization was conditional on an increase in damping or restoring response relative to the increase in noise; no numerical stabilization test was performed, and the condition remained experimentally testable. The anterior stroma differs structurally from the deeper stroma [2]. Depth- and direction-dependent solute transport in the cornea, together with sublayer and hydration assessment by terahertz spectroscopy and imaging, provided an experimental background for depth-resolved validation [29–31]. The QFT version retained anterior localization, but depth remained an empirical/phenomenological input in the present study. In a future field-theory model, the depth itself could become predictive by determining $g_\chi(x)$, $\Gamma_c(x)$, $D_C(x)$, and the effective Marangoni-like stress sensitivity from measured depth-dependent stromal properties. In such a future analysis, a preferred candidate location would be identified by maximizing the independently calibrated transport-efficiency functional; no such maximum was computed in the present study. Such an approach was regarded as a potentially stronger test of the conceptual definition of the HEZ because it would test whether a sub-Bowman peak and axial/radial decay could be reconstructed from data without imposing the simulation reference geometry ($x_0 = 70$ μm, σ = 40 μm) in advance. In practice, coefficients would need to be estimated from depth-resolved measurements of hydration, collagen order, solute mobility, mechanical relaxation, dielectric response, and temperature, and the analysis would then test whether an anterior dissipation maximum emerges without prior specification. In the field model, pathological states could change $\Gamma_c(x)$, $g_\chi(x)$, $D_C(x)$, or effective stress sensitivity. Such changes could alter relaxation spectra, hydration correlations, entropy-normalized transport, and abnormal coupling between the anterior and posterior stroma. QFT was used not to propose "quantum disease," but as a mathematical language

linking microscopic open-system dynamics to measurable mesoscale transport. Clinical significance would arise only if field parameters are shown to discriminate normal from diseased tissue. Self-organization was compatible with the HEZ in the broad sense that structured flows or macroscopic order could emerge from driven dissipative systems [32–34]. Here Γc denotes the selected local channel rate in Eq. (10), not the net solutal linewidth contribution.

The present effective quantum-field formulation may admit nontrivial solutions beyond the simplified local-Markovian calculations. Extensions incorporating nonlinear interactions, stochastic fluctuations, spatially dependent dissipation, and temporal memory could reveal additional dynamical regimes. These may include fluctuation-mediated changes in Marangoni-like stress and transport (Eqs. 19–21); spatial pattern formation through nonlinear interactions (Eq. 3), spatial coupling, and correlated noise (Eq. 30), modulated by local dissipation (Eqs. 10 and 28); depth-dependent transport-to-entropy efficiency maxima (Eq. 27); and history-dependent relaxation arising from memory kernels (Eqs. 33–34). The density-diagonal dephasing channel (Eq. 7) may modulate local damping but cannot independently generate spatial organization. Locally negative contributions to a spatially decomposed Spohn-type diagnostic (Eq. 15) may also arise, although global nonnegativity (Eq. 16) requires appropriate local-Markovian GKLS assumptions and a stationary reference state, and is not guaranteed under memory-kernel extensions. Such local negativity alone would not establish negative physical entropy production, information backflow, or structural ordering. Interactions among these mechanisms could produce qualitatively new responses.

These possibilities remain speculative and were not demonstrated in the present simulations. Their investigation requires physically consistent extensions, independently constrained parameters, appropriate boundary and noise conditions, and experimental validation. Dissipative coefficients should be independently estimated before reconstructing HEZ localization, without imposing the reference geometry (x_0 = 70 μm, σ = 40 μm). A critical test is whether depth-resolved relaxation spectra, linewidths, fluctuation–response relations, correlation times, hydration dynamics, calibrated entropy production (Eq. 18), and entropy-normalized transport quantified by the Endothelial/HEZ Transport Index (EHTI; Eq. 26) exhibit reproducible co-localization beneath Bowman's layer in the anterior stroma. HEZ-off models and matched-integrated-damping controls would distinguish localization effects from overall dissipation. Testing the efficiency maximum (Eq. 27) additionally requires independently calibrated transport fluxes and matched physical entropy budgets. Agreement among independent observables would support the HEZ model, whereas failure to identify the predicted localization or operative stromal stress-to-flow coupling would constrain or potentially falsify its physical interpretation, providing a rigorous basis for evaluating the HEZ–DDS hypothesis.

Conclusion

The corneal HEZ hypothesis was reformulated as a spatially resolved open nonequilibrium effective quantum field theory linking a coarse-grained hydration/proton field, collagen order, and classical solute and temperature variables. Local Lindblad channels and Schwinger–Keldysh kernels supplied a formal description of dissipation, response, fluctuations, and correlations, with anterior localization and solute-dominant Marangoni-like driving retained as phenomenological constraints. Illustrative local-Markovian calculations yielded broader spectral linewidths and shorter first-order correlation times where damping was prescribed to increase; matched-integrated-damping controls yielded distinct local signatures without independently determining HEZ position or physical entropy production. The main contribution is a set of spatial observables, reproducible conditional benchmarks, and prospective criteria for quantitative DDS testing, rather than a demonstration of DDS function or corneal quantum correlations. Beyond offering a possible multiscale explanation of established corneal transport processes, the HEZ formulation may also provide a theoretical basis for identifying previously unrecognized microscopic degrees of freedom and correlation structures. Because the microscopic identity of the collective field and its effective couplings remain undetermined, future investigations may uncover additional collective modes, environmental correlations, or history-dependent dynamics, although these possibilities require independent experimental validation. Future work must identify relevant microscopic modes, measure depth-resolved spectra and correlations, reconstruct spatial dissipation without imposing a Gaussian geometry, and verify coarse-grained stress–transport coupling and the physical entropy budget before quantitatively assessing the HEZ–DDS hypothesis.

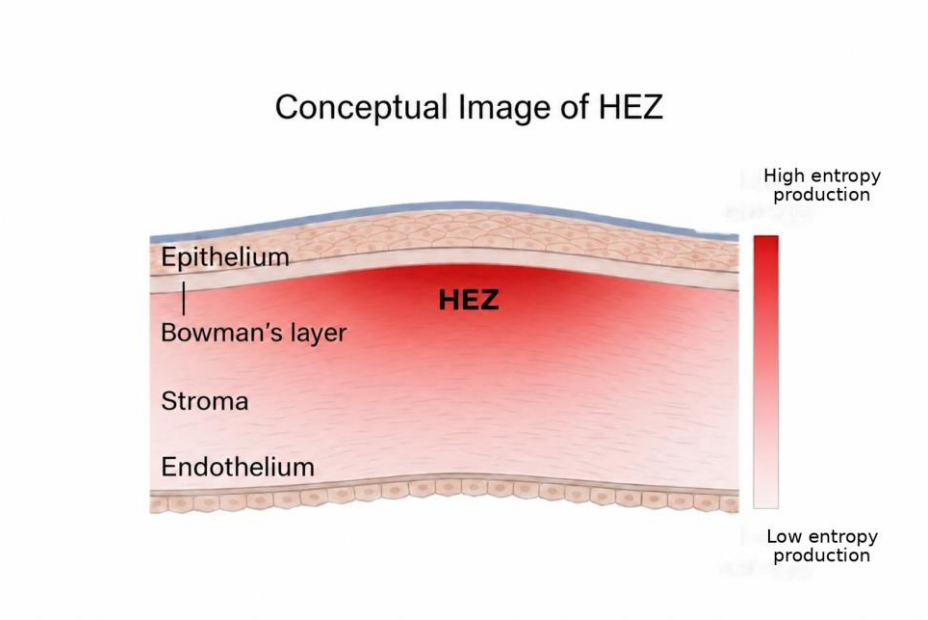


Figure 1. Conceptual spatial organization of the corneal High Entropy-Production Zone (HEZ). The HEZ is represented as an anteriorly biased, anisotropic, quasi-two-dimensional dissipative field with a hypothesized maximum of physical entropy production immediately beneath Bowman's layer and continuous axial decay toward the endothelium and radial decay toward the periphery. It is not a sharply bounded anatomical compartment but a continuous Gaussian-like weighting of hypothesized dissipation and entropy production. In a metaphorical thermodynamic sense, this quasi-two-dimensional layer may also be regarded as quasi-holographic, functionally reflecting or encoding aspects of the three-dimensional stromal transparency state. The color scale denotes hypothesized relative entropy-production intensity, not measured absolute thermodynamic entropy or a measured entropy-production rate. Schematic; not to scale.

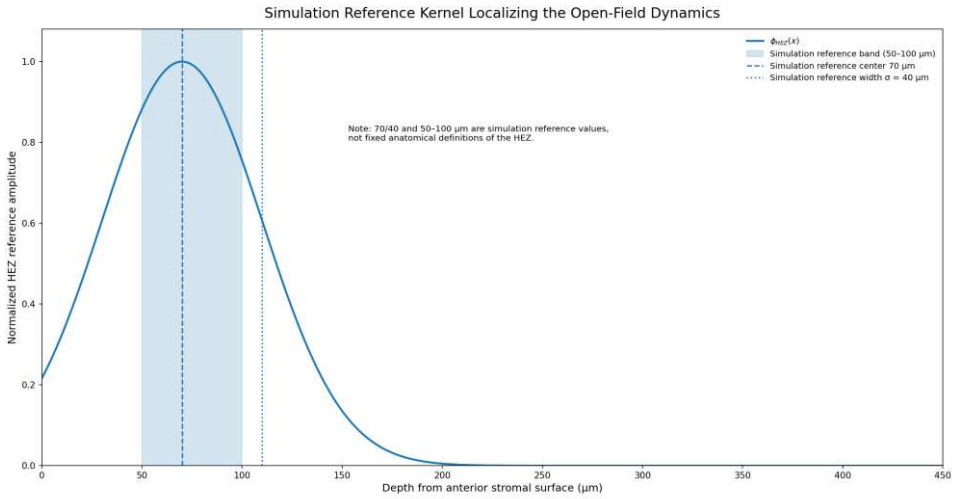


Figure 2. Simulation reference kernel for the HEZ. The Gaussian profile was a numerical implementation inherited from the previous model and did not represent the conceptual or anatomical definition of the HEZ itself. The dashed line at 70 μm indicated the simulation reference center, the characteristic Gaussian width of 40 μm indicated the simulation reference width, and the shaded 50–100 μm region indicated the simulation reference band. The HEZ itself is defined by maximum entropy production immediately beneath Bowman's layer and continuous axial and radial decay from that maximum.

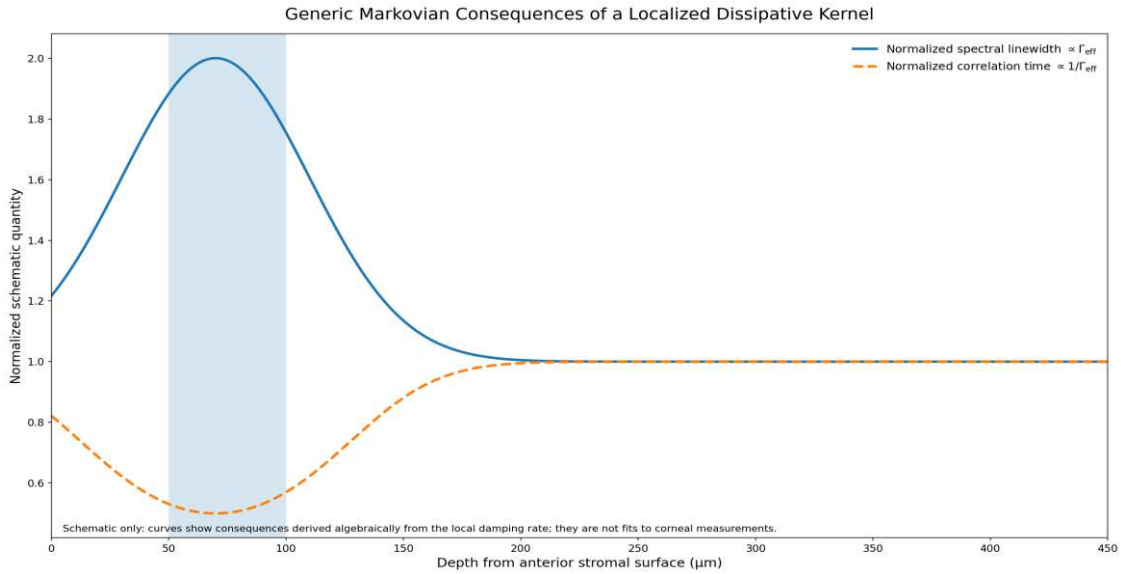


Figure 3. Model-derived numerical results for normalized spectral linewidth and first-order correlation time under an imposed HEZ reference kernel. For the simplest damped-field propagator, the local spectral linewidth was taken to be proportional to Γ_{eff}, while the first-order field-amplitude correlation time was taken to be approximately proportional to $1/\Gamma_{eff}$. The calculated curves used the prescribed Gaussian reference center of 70 μm, width of 40 μm, and unit damping modulation; at the imposed center the normalized linewidth was 2.0 and the first-order correlation time was 0.5. They were illustrative numerical outputs, not fits to corneal measurements, independently determined HEZ localization, or estimates of physical entropy production.

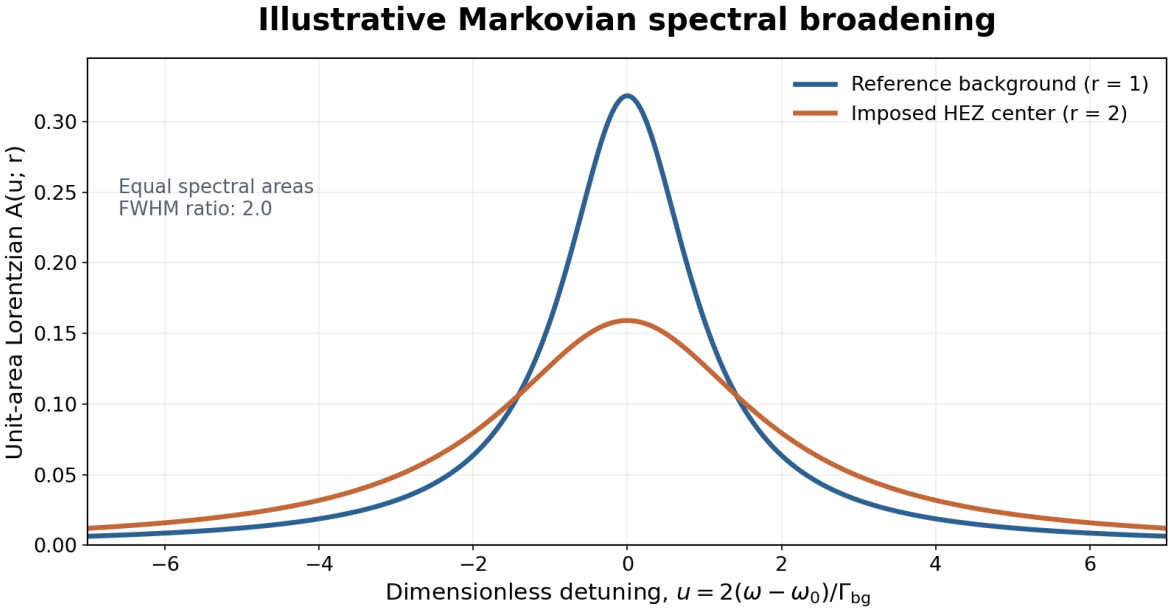


Figure 4. Illustrative normalized Lorentzian spectral line shapes generated from the local-Markovian damping relation. The nominal background (r = 1) and imposed HEZ reference center (r = 2) were calculated using the equal-area function A(u; r) = r/[π(u² + r²)] with common resonance frequency and the corrected dimensionless detuning u = 2(ω − ω₀)/Γbg, where Γbg is the baseline angular-frequency FWHM. The center spectrum had twice the reference full width at half maximum and half the peak height by construction. Both frequency and intensity are dimensionless; the curves were analytical illustrations, not fitted spectra or simulations of a microscopic corneal quantum mode.

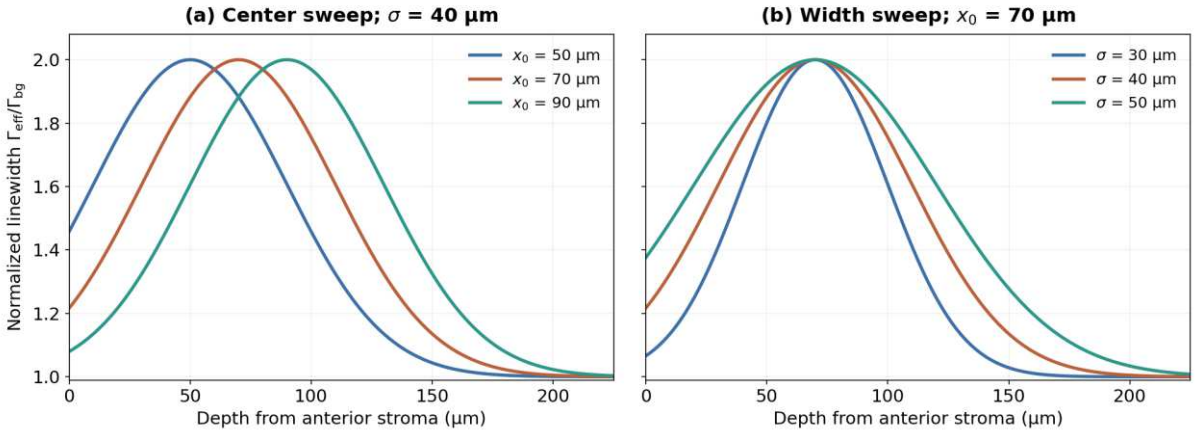


Figure 5. Sensitivity of the illustrative normalized linewidth profile to the prescribed Gaussian reference geometry. (a) The center x_0 was varied among 50, 70, and 90 µm at fixed width σ = 40 µm. (b) The width σ was varied among 30, 40, and 50 µm at fixed center x_0 = 70 µm. The same imposed rule $\Gamma eff/\Gamma bg = 1 + \varphi(x; x_0, \sigma)$ was evaluated across the full 0–450 µm depth; the anterior 0–225 µm interval was displayed for readability. These sensitivity curves did not infer anatomical localization from independent corneal measurements.

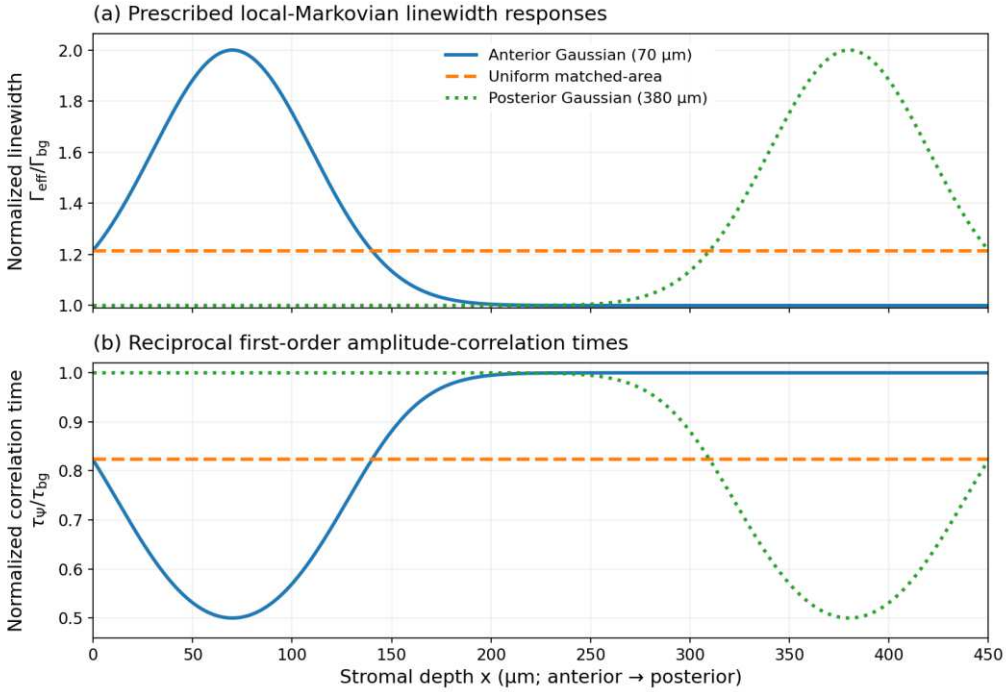


Figure 6. Matched-integrated-excess-damping spatial controls using the same prescribed local-Markovian scaling as Figure 3. The anterior Gaussian (center 70 µm, width 40 µm), a uniform control, and a mirrored posterior Gaussian (center 380 µm, width 40 µm) were normalized to equal $\int_0^{450} \varphi(x)\,dx$ = 96.249 µm. (a) Normalized spectral linewidth $\Gamma eff/\Gamma bg = 1 + \varphi(x)$. (b) Normalized first-order field-amplitude correlation time $\tau\Psi/\tau bg = [1 + \varphi(x)]^{-1}$. Their different depth profiles were entirely determined by the assigned kernels; the matched quantity was integrated excess normalized damping, not independently calibrated physical entropy production. No experimental corneal observations or inverse reconstruction were used.

Tables

Table 1. Overview of the Field-Theoretic Method

Methodological Component	Field-Theoretic Content	Status / Constraint
Spatial HEZ kernel	Gaussian HEZ reference weighting $\varphi_{HEZ}(x)$; see Eq. (1)	Simulation reference geometry: $x_0 = 70$ μm; $\sigma = 40$ μm
Classical driving (not simulated)	Prescribed concentration and temperature gradients; no direct fluid-transport solve	Phenomenological background; not a numerical flow model
Collective quantum field	Coarse-grained bosonic hydration/proton collective field	New effective degree of freedom
Stromal order field	$\chi(\mathbf{x}, t)$	Semiclassical in the minimal model
Conservative dynamics	Nonrelativistic effective Hamiltonian	Couplings remain symbolic except for inherited values
Dissipation	Local-field Lindblad channels $L_{\phi}, L_{\text{loss}}, L_{\text{gain}}$	Markov approximation; local rates nonnegative and loss > gain for stable linear bosonic occupation
Nonequilibrium QFT	Schwinger-Keldysh response/noise action; first-order and connected density correlations (Eqs. 22–23)	Quadratic/linearized response and noise kernels; no full QFT evolution simulated
Entropy production	Local Spohn diagnostic $\sigma_q(x,t)$; matched physical entropy $\sigma_{\text{phys,matched}}(x,t)$; classical flux–affinity entropy-production candidate (Eq. 17)	Spohn relaxation and independently calibrated physical entropy production are distinct; avoid double counting; classical and Spohn contributions are not naively additive
Marangoni-like coupling	$\gamma_{\text{eff}}[C, T, \chi, \langle n \rangle, \mathcal{C}_{2,a}]$	Phenomenological stress proxy; hydrodynamic/poroelastic closure not derived
Efficiency	EHTI_{QFT}; prospective candidate-position gain functional (Eq. 27)	Operational flux/cost ratio: fixed units, positive physical denominator, no double counting; location optimum not calculated
Matched-damping spatial control (Figure 6)	Anterior Gaussian, equal-area uniform, mirrored posterior Gaussian; common integrated excess damping	Deterministic sensitivity/control calculation; assumed spatial kernels, no measured corneal localization or matched physical entropy production

Table 2. Integrated Comparison of the Classical HEZ, Finite-Dimensional Quantum HEZ, and Quantum-Field HEZ

Feature	Classical HEZ (Reference 4)	Two-level quantum HEZ (Reference 5)	Open-QFT HEZ (Present study)	Interpretation
Primary domain	Continuum transport	Local open quantum subsystem	Spatially extended open field	Improved spatial/mode resolution
State variables	Concentration, temperature, velocity	Density matrix $\rho(t)$	Field density operator / Keldysh field	Generalization to multiple modes
Definition of the HEZ	Continuous entropy-production field with a maximum immediately beneath Bowman's layer and axial/radial decay	Localized quantum subsystem embedded in the same conceptual HEZ field	The same conceptual HEZ field represented by localized Hamiltonian/dissipative kernels	Separates conceptual definition from numerical parameterization
Entropy and dissipation	Classical flux–affinity entropy production	von Neumann entropy; Spohn relaxation	Spatial Spohn diagnostic; independently matched physical entropy budget	Do not simply add classical and quantum contributions
Primary driving hierarchy	Solutal > thermal	Solutal > thermal	Coupling hierarchy constrained to preserve solute dominance	Phenomenological until calibrated
Role of heat	Stabilization / damping	Thermal decoherence channel	Damping / noise kernel	Testable through response and fluctuations
Spatial location	Sub-Bowman peak + axial/radial decay	Same conceptual definition; x_0 = 70 μm and σ = 40 μm are simulation reference geometry	Same conceptual definition; $x_0 = 70$ μm and σ = 40 μm are simulation reference geometry	50-100 μm is also a simulation reference band, not a definition or measured value
New observables	Flow, concentration, stress	Entropy, decoherence	$G^R, G^K, A\Psi(k,\omega), \tau_{corr}, \xi_{corr}$	Adds falsifiability

Feature	Classical HEZ (Reference 4)	Two-level quantum HEZ (Reference 5)	Open-QFT HEZ (Present study)	Interpretation
Information interpretation	Not explicit	Local coherence reduction	Redistribution into environment/correlations	Avoids a claim of fundamental information destruction
Efficiency index	EHTI_{cl}	EHTI_{q}	EHTI_{QFT}	Operational flux/cost ratio; fixed units and positive physical denominator required

Table 3. Depth-Resolved Numerical Values from the Imposed HEZ Reference Kernel

Depth x (μm)	Reference kernel φ(x)	Linewidth Γeff/Γbg	Correlation time τΨ/τbg
0	0.216	1.216	0.822
30	0.607	1.607	0.622
50	0.882	1.882	0.531
70	1.000	2.000	0.500
100	0.755	1.755	0.570
150	0.135	1.135	0.881
200	0.005	1.005	0.995

Note. Values were calculated using $x_0 = 70$ μm and $\sigma = 40$ μm and rounded to three decimals. All columns are dimensionless except depth. The 70 μm center and Gaussian width were prescribed; the table is not an independent prediction of corneal HEZ position or an experimentally calibrated thermodynamic entropy budget.

References

1. Edelhauser HF. The balance between corneal transparency and edema: The Proctor Lecture. Invest Ophthalmol Vis Sci. 2006;47:1754–1767. doi:10.1167/iovs.05-1139.
2. Abass A, Hayes S, White N, Sorensen T, et al. Transverse depth-dependent changes in corneal collagen lamellar orientation and distribution. J R Soc Interface. 2015;12(104):20140717. doi:10.1098/rsif.2014.0717.
3. Meek KM, Knupp C. Corneal structure and transparency. Prog Retin Eye Res. 2015;49:1–16. doi:10.1016/j.preteyeres.2015.07.001.
4. Sonoda Y. High Entropy-Production Zone (HEZ) and Marangoni Effect-Driven Convection: A Hypothesis for Corneal Stromal Dynamics. Research Square [Preprint]. 2025. doi:10.21203/rs.3.rs-7456650/v2.
5. Sonoda Y. Quantum-Classical Consistency of Entropy Dissipation and Convection in the High Entropy-Production Zone (HEZ) of the Corneal Stroma. Research Square [Preprint]. 2026. doi:10.21203/rs.3.rs-7633016/v2.
6. Manzano D. A short introduction to the Lindblad master equation. AIP Adv. 2020;10:025106. doi:10.1063/1.5115323.
7. Landi GT, Paternostro M. Irreversible entropy production: From classical to quantum. Rev Mod Phys. 2021;93:035008. doi:10.1103/RevModPhys.93.035008.
8. Kamenev A, Levchenko A. Keldysh technique and non-linear **σ**-model: basic principles and applications. Adv Phys. 2009;58:197–319. doi:10.1080/00018730902850504.
9. Thompson F, Kamenev A. Field theory of many-body Lindbladian dynamics. Ann Phys. 2023;455:169385. doi:10.1016/j.aop.2023.169385.
10. de Vega I, Alonso D. Dynamics of non-Markovian open quantum systems. Rev Mod Phys. 2017;89:015001. doi:10.1103/RevModPhys.89.015001.
11. Marino J, Diehl S. Driven Markovian quantum criticality. Phys Rev Lett. 2016;116:070407. doi:10.1103/PhysRevLett.116.070407.
12. Sieberer LM, Buchhold M, Diehl S. Keldysh field theory for driven open quantum systems. Rep Prog Phys. 2016;79:096001. doi:10.1088/0034-4885/79/9/096001.
13. Huelga SF, Plenio MB. Vibrations, quanta and biology. Contemp Phys. 2013;54:181–207. doi:10.1080/00405000.2013.829687.
14. Brookes JC. Quantum effects in biology: golden rule in enzymes, olfaction, photosynthesis and magnetodetection. Proc R Soc A. 2017;473:20160822. doi:10.1098/rspa.2016.0822.
15. Lambert N, Chen YN, Cheng YC, et al. Quantum biology. Nat Phys. 2013;9:10–18. doi:10.1038/nphys2474.
16. Iida H, Kunihiro T, Müller B, et al. Entropy production in classical Yang–Mills theory from Glasma initial conditions. Phys Rev D. 2013;88:094006. doi:10.1103/PhysRevD.88.094006.
17. Ptaszyński K, Esposito M. Quantum and classical contributions to entropy production in fermionic and bosonic Gaussian systems. PRX Quantum. 2023;4(2):020353. doi:10.1103/PRXQuantum.4.020353.
18. Müller B, Schäfer A. Entropy production in high energy processes. arXiv:hep-ph/0306309v2 [hep-ph]. 2003.
19. Goold J, Huber M, Riera A, et al. The role of quantum information in thermodynamics—a topical review. J Phys A Math Theor. 2016;49:143001. doi:10.1088/1751-8113/49/14/143001.
20. Park S, Liu L, Demirkır Ç, et al. Solutal Marangoni effect determines bubble dynamics during electrocatalytic hydrogen evolution. Nat Chem. 2023;15:1532–1540. doi:10.1038/s41557-023-01294-y.
21. Johansson P, Galliéro G, Legendre D. How molecular effects affect solutal Marangoni flows. Phys Rev Fluids. 2022;7:064202. doi:10.1103/PhysRevFluids.7.064202.
22. Babich A, Mutschke G, Bashkatov A, et al. Solutal Marangoni convection at growing oxygen bubbles during water electrolysis. Phys Rev Res. 2025;7:023189. doi:10.1103/PhysRevResearch.7.023189.
23. Craster RV, Matar OK. Dynamics and stability of thin liquid films. Rev Mod Phys. 2009;81:1131–1198. doi:10.1103/RevModPhys.81.1131.

24. Caprini L, Löwen H, Geilhufe RM. Ultrafast entropy production in pump-probe experiments. Nat Commun. 2024;15:94. doi:10.1038/s41467-023-44277-w.

25. Täuber UC, Howard M, Vollmayr-Lee BP. Applications of field-theoretic renormalization group methods to reaction–diffusion problems. J Phys A Math Gen. 2005;38:R79–R131. doi:10.1088/0305-4470/38/17/R01.

26. Breuer HP, Laine EM, Piilo J, et al. Colloquium: Non-Markovian dynamics in open quantum systems. Rev Mod Phys. 2016;88:021002. doi:10.1103/RevModPhys.88.021002.

27. Rivas Á, Huelga SF, Plenio MB. Quantum non-Markovianity: characterization, quantification and detection. Rep Prog Phys. 2014;77:094001. doi:10.1088/0034-4885/77/9/094001.

28. Fanchini FF, Werlang T, Brasil CA, et al. Non-Markovian dynamics of quantum discord. Phys Rev A. 2010;81:052107. doi:10.1103/PhysRevA.81.052107.

29. Hepfer RG, Chen P, Shi C, et al. Depth- and direction-dependent changes in solute transport following cross-linking with riboflavin and UVA light in ex vivo porcine cornea. Exp Eye Res. 2021;205:108498. doi:10.1016/j.exer.2021.108498.

30. Ke L, Wu QYS, Zhang N, et al. Terahertz spectroscopy analysis of human corneal sublayers. J Biomed Opt. 2021;26:043011. doi:10.1117/1.JBO.26.4.043011.

31. Chow BJ, Liu C, Yu M, et al. The application of terahertz technology in corneas and corneal diseases: A systematic review. Bioengineering. 2025;12(1):45. doi:10.3390/bioengineering12010045.

32. Goldbeter A. Dissipative structures in biological systems: bistability, oscillations, spatial patterns and waves. Philos Trans A Math Phys Eng Sci. 2018;376:20170376. doi:10.1098/rsta.2017.0376.

33. Karsenti E. Self-organization in cell biology: a brief history. Nat Rev Mol Cell Biol. 2008;9:255–262. doi:10.1038/nrm2357.

34. Pulselli RM, Simoncini E, Tiezzi E. Self-organization in dissipative structures: A thermodynamic theory for the emergence of prebiotic cells and their epigenetic evolution. Biosystems. 2009;96:237–241. doi:10.1016/j.biosystems.2009.02.004.

Declarations

Ethics approval and consent to participate

Not applicable. This study does not involve human participants, human tissue, or animal subjects.

Consent for publication

Not applicable.

Competing interests

The author declares no competing interests.

Funding

The author received no specific funding for this work.

Statement on AI use and author responsibility

In this manuscript, ChatGPT (OpenAI; GPT-6) was used as an assistive tool to support mathematical formulation based on an open nonequilibrium effective quantum-field approach, as well as the preparation and consistency checking of illustrative numerical calculations, figures, and accompanying reproducibility code. The author carefully reviewed, revised, and approved the final manuscript and retains full responsibility for its scientific content and final presentation.

Supplementary Material — Baseline Quantum-Field-Theory Formulation and Reproducibility Map

S0. Purpose of the Supplementary Material

This Supplementary Material maps the baseline parameters of the previous HEZ manuscript onto the notation of the effective field theory and distinguishes the following three categories.

1. Inherited parameters: quantities retained directly from the prior document on which this manuscript is based.
2. Mapped phenomenological parameters: quantities such as the dephasing and relaxation rates from the previous model that are reused only as assumed simulation reference scales for the local-field dissipators, not as experimentally measured corneal rates.
3. New QFT coefficients: quantities left symbolic because the source materials contain no experimental or microscopic numerical values for them.

This distinction is important for reproducibility and interpretation; no numerical values are assigned to new QFT coefficients without calibration. Section S8 further documents a reproducible, post hoc implementation of the deterministic reference calculations reported in Figures 2–5 and Table 3.

S1. HEZ Simulation Reference Kernel

To implement the conceptual definition of the HEZ in a one-dimensional numerical model, the following dimensionless spatial-localization function is used as the simulation reference kernel.

$$\phi_{\mathrm{HEZ}}(x) = A_{\mathrm{HEZ}}\exp\left[-\frac{(x-x_0)^2}{2\sigma^2}\right], \tag{S1}$$

Here $A_{\mathrm{HEZ}} = 1$, $x_0 = 70$ µm, and $\sigma = 40$ µm. $x_0 = 70$ µm and σ = 40 µm are the simulation reference geometry inherited from the prior document and do not represent the conceptual definition of the HEZ, a fixed anatomical position, boundary, or width, or a measured center depth or width. The conceptual definition of the HEZ is instead specified by maximum entropy production immediately beneath Bowman's layer and continuous axial and radial decay away from that maximum. The inherited simulation reference parameters are listed in Table S1.

Table S1. Inherited Simulation Reference Parameters

Parameter	Symbol	Baseline Value	Unit	Status / Note
Stromal slab thickness	L	450	µm	Inherited one-dimensional reference geometry
Simulation reference center	x_0	70	µm	Reference geometry; not a fixed HEZ definition or measured center depth
Simulation reference width	σ	40	µm	Reference geometry; not a fixed HEZ definition or measured width
Solute diffusion coefficient	D_C	500	µm²/s	Inherited conceptual value
Temperature gradient	$\lvert\nabla T\rvert$	0.002	K/µm	Inherited baseline gradient
Solute concentration difference	ΔC	1.0	mM	Inherited central-peripheral baseline difference

S2. Field Variables and Their Interpretation

The effective field components and their interpretations are summarized in Table S2.

Table S2. Effective Field Components

Quantity	Symbol	Type	Interpretation	Numerical Value
Collective hydration/proton field	$\hat{\Psi}(\mathbf{x}, t)$	Quantum field	Coarse-grained microscopic/mesoscale mode	Not fixed
Collective density	$\hat{n} = \hat{\Psi}^{\dagger}\hat{\Psi}$	Operator	Local occupation/intensity of the retained field	Derived quantity
Collagen order	$\chi(\mathbf{x}, t)$	Real semiclassical field	Slow stromal structural order	Not fixed
Solute concentration	$C(\mathbf{x}, t)$	Classical field	Concentration/osmotic driving	Inherited from the previous model; not independently calibrated here
Temperature	$T(\mathbf{x}, t)$	Classical field	Thermal driving	Inherited from the previous model; not independently calibrated here
HEZ localization	$\phi_{HEZ}(x)$	Prescribed dimensionless field	Spatial weighting of couplings	Fixed by S1

The effective fields are not macroscopic coherent wavefunctions but coarse-grained operator fields defined at the chosen ultraviolet cutoff. The dephasing and energy-relaxation rates associated with this model are illustrative assumptions inherited from Reference 5, not measured properties of corneal tissue; their mapping is described in Section S4 and Eq. (S2).

S3. Conservative QFT Parameters

The effective Hamiltonian contains the coefficients m_{eff}, μ_{eff}, u, g_{χ}, g_{C}, g_{T}, g_{H}, κ_{χ}, r_{χ}, v_{χ}, and h_{χ}. No physiological numerical value is assigned to any of these coefficients in this manuscript. The new conservative coefficients requiring calibration are listed in Table S3. A representative polynomial convention is $V\chi(\chi) = (r\chi/2)\chi^2 + (v\chi/4)\chi^4 - h\chi\chi$ with $v\chi > 0$; the coefficients remain uncalibrated and the chosen truncation is illustrative.

Table S3. New Conservative Coefficients Requiring Calibration

Parameter	Symbol	Role	Status
Effective field mass/stiffness	m_{eff}	Dispersion of Ψ	Uncalibrated
Effective chemical potential	μ_{eff}	Controls mean occupation	Uncalibrated

Parameter	Symbol	Role	Status
Local self-interaction	u	Nonlinear field coupling	Uncalibrated
Collagen-field coupling	g_χ	Couples Ψ to stromal order	Uncalibrated
Solute-field coupling	g_C	Couples Ψ and C	Uncalibrated
Thermal-field coupling	g_T	Couples Ψ and T	Uncalibrated
HEZ potential coupling	g_H	Couples Ψ to the HEZ profile	Uncalibrated
Collagen gradient stiffness	κ_χ	Suppresses sharp spatial variation	Uncalibrated
Landau coefficients	r_χ, v_χ, h_χ	Effective collagen-order potential	Uncalibrated

Future microscopic studies or inverse modeling will be required to identify the necessary terms; the present list is a minimal candidate basis rather than a final Hamiltonian.

S4. Dissipative Parameters and Mapping from the Previous Model

The preceding two-level model (Reference 5) adopted a dephasing rate $\gamma = 10^3\ \mathrm{s}^{-1}$ and an energy-relaxation rate $\kappa = 10^2\ \mathrm{s}^{-1}$. These numerical rates were assumed for illustrative simulations in Reference 5; neither rate was obtained from an experimental measurement in corneal tissue. In the present field formulation, the values are carried forward only as phenomenological simulation reference scales, without independent empirical calibration.

$$\Gamma_{\phi,ref} = 10^3\ \mathrm{s}^{-1}, \qquad \Gamma_{\mathrm{loss},ref} = 10^2\ \mathrm{s}^{-1}. \tag{S2}$$

The values mapped in Eq. (S2) remain simulation-only assumptions inherited from Reference 5, not experimentally measured or validated rates of corneal dephasing, energy relaxation, or local field dynamics. With the continuum field normalization used in the main text, the dephasing operator includes the finite-cell factor a^3 under the square root so that $\Gamma\phi,\mathrm{ref}$ retains units of s^{-1}. The dissipative channels in the field formulation are summarized in Table S4. The gain reference is intentionally unspecified, so no full-rank stationary state was inferred from these baseline scales. To use the logarithmic Spohn functional of Eqs. (15–16), a faithful stationary reference state must be independently established for the chosen finite-cutoff dynamics; in a simple single-mode linear loss–gain sector this holds for $\Gamma\mathrm{loss} > \Gamma\mathrm{gain} > 0$, but not for the pure-vacuum limit $\Gamma\mathrm{gain} = 0$.

Table S4. Dissipative Field Channels

Channel	Operator	Baseline Scale	Physical Role	Calibration Status
Dephasing	$\hat{L}_\phi = \sqrt{\Gamma_\phi\, a^3}\,\hat{n}$	$10^3\ \mathrm{s}^{-1}$	Loss of local phase information	Assumed simulation value from Reference 5; not experimentally measured
Relaxation	$\hat{L}_{\mathrm{loss}} = \sqrt{\Gamma_{\mathrm{loss}}}\,\hat{\Psi}$	$10^2\ \mathrm{s}^{-1}$	Loss/relaxation to the environment	Assumed simulation value from Reference 5; not experimentally measured
Injection	$\hat{L}_{\mathrm{gain}} = \sqrt{\Gamma_{\mathrm{gain}}}\,\hat{\Psi}^\dagger$	Unspecified	Nonequilibrium repopulation	New; uncalibrated

Channel	Operator	Baseline Scale	Physical Role	Calibration Status
Solute modulation	$\lambda_c^C \mathcal{F}_C$	Unspecified	Gradient-dependent dissipation	New; qualitative hierarchy inherited
Thermal modulation	$\lambda_c^T \mathcal{F}_T$	Unspecified	Damping/noise modulation	New; qualitative stabilizing role inherited
HEZ modulation	$\lambda_c^H \phi_{HEZ}$	Unspecified	Localizes enhanced dissipation	New parameter on inherited geometry

S5. Baseline Numerical Grid and Stability Notes

The numerical parameters inherited from the previous model were retained solely for traceability and are summarized in Table S5.

Table S5. Conventional Numerical Parameters Retained for Traceability

Parameter	Symbol	Original-Model Baseline Value	Unit	QFT Note
Spatial step	Δx	1.0	μm	May serve as a coarse-graining cutoff in lattice implementations
Time step	Δt	10^{-3}	s	Must be revalidated for QFT-solver stability
Number of steps	N	100000	–	Conventional value; not proof of QFT convergence
Anterior boundary	–	$T = T_0 + \Delta T/2, C = C_0 + \Delta C/2$	–	Inherited classical boundary condition
Posterior boundary	–	$\partial_n T = 0, \partial_n C = 0$	–	Inherited no-flux condition
Initial solute profile	$C(x,0)$	Gaussian centered at x_0	mM	Inherited
Initial temperature	$T(x,0)$	Linear gradient	K	Inherited

Field-theoretic calculations should include convergence tests with respect to Δx, Δt, system size, and the ultraviolet cutoff. Stochastic Keldysh simulations should also demonstrate ensemble convergence.

Time-step resolution and convergence. The inherited step $\Delta t = 10^{-3}$ s and dephasing reference $\Gamma\phi,\mathrm{ref} = 10^3$ s^{-1} yield $\Gamma\phi,\mathrm{ref}\,\Delta t = 1$. Consequently the historical grid cannot be assumed to resolve the fastest dephasing dynamics accurately. An explicit solver should be tested using progressively smaller Δt (for example, orders of magnitude below $1/\Gamma\phi,\mathrm{ref}$ where feasible), while implicit, exponential, or completely-positive integrators require their own error and stability checks. Numerical convergence must be assessed for coherence, number relaxation, spectra, and noise statistics separately; stability of a chosen algorithm does not itself prove temporal accuracy. Because the inherited dephasing and energy-relaxation reference rates are simulation assumptions rather than measured corneal parameters, this time-step assessment addresses numerical resolution only and does not establish physiological relaxation times.

S6. Recommended Field-Theoretic Observables

The field-theoretic observables recommended for future studies are summarized in Table S6.

Table S6. Observable Set for Future Numerical or Experimental Studies

Observable	Definition / Proxy	Scientific Question
Retarded response	$G^R(k,\omega;x)$	How does the collective mode respond to perturbation?
Spectral function	$A_\Psi = -2\,\mathrm{Im}\,G^R$	Does the linewidth increase in the HEZ?
Keldysh correlation function	G^K	How strong are the nonequilibrium fluctuations?
Correlation time	τ_Ψ	Is relaxation accelerated in the HEZ?
Correlation length	ξ_Ψ	Is spatial coherence shortened or reorganized?
Local Spohn relaxation diagnostic	$\sigma_q(x,t)$	How does the relative-entropy relaxation diagnostic vary with depth?
Matched physical entropy production	$\sigma_{\mathrm{phys,matched}}(x,t)$	Is independently calibrated physical dissipation localized?
Effective Marangoni-like stress proxy	$\tau_M = \nabla_s \gamma_{eff}$	Do field fluctuations couple to transport?
Entropy-normalized efficiency	EHTI_{QFT}	Does the HEZ improve useful flux per dissipative cost?
Noise-response ratio	$G^K/(G^R - G^A)$ or an appropriate generalization	How far from equilibrium is the local field?

S7. Matched-Integrated-Excess-Damping Numerical Control

Figure 6 compared three prescribed, nonnegative, dimensionless spatial modulation kernels over the illustrative stromal interval $0 \le x \le L = 450$ μm. The anterior Gaussian and its mirrored posterior control were defined as follows:

$$\phi_A(x) = \exp\left[-\frac{(x - 70\,\mu\mathrm{m})^2}{2(40\,\mu\mathrm{m})^2}\right]$$

$$\phi_P(x) = \exp\left[-\frac{(x - 380\,\mu\mathrm{m})^2}{2(40\,\mu\mathrm{m})^2}\right] = \phi_A(L - x)$$

The uniform control was normalized to the same depth-integrated excess as the anterior Gaussian:

$$I_A \equiv \int_0^L \phi_A(x)\,dx \approx 96.2486\,\mu\mathrm{m}, \qquad \phi_U(x) = \frac{I_A}{L} \approx 0.213886$$

Since the posterior Gaussian is the mirror image of the anterior Gaussian on the same interval, all three kernels have an identical depth integral:

$$\int_0^L \phi_A(x)\,dx = \int_0^L \phi_P(x)\,dx = \int_0^L \phi_U(x)\,dx = I_A$$

For each profile i ∈ {A, U, P}, we used the same prescribed local-Markovian normalization as in Figure 3, with Γbg and τbg denoting the background linewidth and first-order field-amplitude correlation time:

$$r_i(x) \equiv \frac{\Gamma_{\mathrm{eff},i}(x)}{\Gamma_{\mathrm{bg}}} = 1 + \phi_i(x), \qquad \frac{\tau_{\psi,i}(x)}{\tau_{\mathrm{bg}}} = \frac{1}{r_i(x)}$$

Each function was sampled at 0.01-μm intervals over the full 0–450-μm slab, and integrals were evaluated with the composite trapezoidal rule:

$$x_j = j\,\Delta x, \qquad \Delta x = 0.01\,\mu\mathrm{m}, \qquad j = 0,1,\ldots,45000$$

To quantify anterior localization, we calculated the fraction of each integrated modulation lying in the 0–150-μm interval:

$$F_i(0\text{–}150\,\mu\mathrm{m}) \equiv \frac{\int_0^{150\,\mu\mathrm{m}} \phi_i\,(x)\,dx}{\int_0^{L} \phi_i\,(x)\,dx}$$

The resulting dimensionless anterior fractions were:

$$F_A = 0.9763005, \qquad F_U = 0.3333333, \qquad F_P \approx 4.65 \times 10^{-9}$$

Equivalently, the spatial integral of excess normalized linewidth was held fixed for every control profile:

$$\int_0^{L} [r_i(x) - 1]\;dx = \int_0^{L} \phi_i\,(x)\,dx = I_A$$

The matched quantity is the depth integral of the imposed normalized linewidth excess, not reservoir-resolved thermodynamic dissipation or physical entropy production. These deterministic outputs retain the prescribed positional information but do not independently identify an HEZ, infer its anatomical location, calculate biological transport, or solve the full quantum-field dynamics.

S8. Reproducible Numerical Simulation Protocols for Figures 2–5 and Table 3

This section documents the deterministic calculations that generated the illustrative spatial profiles and line shapes in Figures 2–5 and the sampled values in Table 3. The corresponding matched-integrated-excess-damping control for Figure 6 is specified in Section S7 and is cross-checked in the companion reference implementation. These procedures reproduce consequences of prescribed mathematical inputs; they do not constitute a direct numerical solution of the full Lindblad or Schwinger–Keldysh field evolution, a fit to corneal data, or an independent inference of HEZ anatomy.

S8.1. Numerical assumptions, reference values, and provenance

The depth coordinate x is expressed in micrometers, with $x = 0$ at the anterior boundary and $x = 450\,\mu$m at the posterior boundary of the illustrative one-dimensional stromal slab. The prescribed Gaussian reference center is $x_0 = 70\,\mu$m, its characteristic width is $\sigma = 40\,\mu$m, and its dimensionless peak amplitude is unity. The linewidth enhancement is set to $\frac{\Delta\Gamma}{\Gamma_{\mathrm{bg}}} = 1$ as an illustrative input; Γ_{bg} and τ_{bg} are normalization baselines rather than independently measured physical rates. No absolute spectral frequency, laboratory time scale, or calibrated corneal noise spectrum is required to evaluate the normalized curves.

S8.2. Gaussian reference-profile calculation (Figure 2)

Evaluate the dimensionless spatial-localization kernel of Eq. (1) at each selected depth with the prescribed center and width:

$$\varphi(x; x_0, \sigma) = \exp\left[-\frac{(x-x_0)^2}{2\sigma^2}\right].$$

Set $x_0 = 70\,\mu$m and $\sigma = 40\,\mu$m, and plot $\varphi(x)$ against x over 0–450 μm. The maximum is exactly $\varphi(x_0) = 1$ and the profile decreases continuously away from its imposed center. The curve is an input profile, not an inference of the HEZ position or a measurement of entropy production. No parameter fitting or data-based normalization is performed.

S8.3. Local-Markovian linewidth and correlation-time responses (Figure 3; Table 3)

Starting from the same Gaussian profile, evaluate the prescribed local effective-linewidth ratio $r(x)$ and the first-order field-amplitude correlation-time ratio $t(x)$ using Eqs. (13), (24), and the numerical procedure described under Methods, Section 6:

$$r(x) \equiv \frac{\Gamma_{\mathrm{eff}}(x)}{\Gamma_{\mathrm{bg}}} = 1 + \varphi(x); \quad t(x) \equiv \frac{\tau_\Psi(x)}{\tau_{\mathrm{bg}}} = \frac{1}{r(x)}.$$

Plot $r(x)$ and $t(x)$ over the depth domain. Independently evaluate these analytic expressions at $x = 0, 30, 50, 70, 100, 150,$ and $200\,\mu$m to reproduce Table 3. Calculate at full floating-point precision and round only the displayed values to three decimals. At the imposed center, $\varphi = 1$, $r = 2.000$, and $t = 0.500$; at 50 μm, the corresponding displayed values are 0.882, 1.882, and 0.531, and at 100 μm they are 0.755, 1.755, and 0.570. The reciprocal time relation presumes a stationary single-pole local-Markovian field-amplitude correlation; it does not represent density relaxation or a measured corneal correlation time.

S8.4. Equal-area Lorentzian spectral illustration (Figure 4)

For the illustrative line-shape comparison, define the dimensionless detuning $u = \frac{2(\omega-\omega_0)}{\Gamma_{\mathrm{bg}}}$, keep ω_0 fixed, and calculate the following Lorentzian for the two prescribed linewidth ratios $r = 1$ (background) and $r = 2$ (Gaussian reference maximum):

$$L(u;r) = \frac{r}{\pi(u^2+r^2)}.$$

The integral of L over the complete real u axis equals unity by construction. Its peak height is $L(0;r) = \frac{1}{\pi r}$, while its dimensionless full width at half maximum is $\mathrm{FWHM}_u = 2r$ (equivalently, angular-frequency $\mathrm{FWHM}_\omega = r\Gamma_{\mathrm{bg}}$). Thus, when r changes from 1 to 2, the FWHM doubles and the peak height halves. A finite plotting interval approximates the unbounded line shape but does not itself contain exactly unit area. The independent reference script uses a symmetric display window of $-12 \le u \le 12$ as a visualization choice, not an assertion about the original figure axis limits. $L(u;r)$ is the separate normalized illustration, not the field spectral function $A_\Psi(k,\omega;x)$ of Eq. (25).

S8.5. Geometry-sensitivity analysis (Figure 5)

Repeat the normalized-linewidth computation $r(x) = 1 + \varphi(x;x_0,\sigma)$ for two one-factor-at-a-time sweeps. In Figure 5a, vary x_0 across 50, 70, and 90 μm while holding $\sigma = 40\,\mu$m. In Figure 5b, vary σ across 30, 40, and 50 μm while holding $x_0 = 70\,\mu$m. Keep the modulation amplitude at unity in both sweeps and display the anterior 0–225 μm interval to resolve the imposed variations. The maximum $r(x_0)$ remains 2 in every case, and the center changes only when x_0 is changed. For a Gaussian excess profile, the analytical spatial FWHM is $2\sqrt{2\ln 2}\,\sigma$, giving approximately 70.6, 94.2, and 117.7 μm for σ = 30, 40, and 50 μm. These outputs quantify sensitivity to input geometry rather than identify a physiologically preferred HEZ depth or width.

S8.6. Reproduction checks, code provenance, and scientific limits

The supplied independent reference implementation reproduces the formulas above, exports the Table 3 values to a comma-separated table, generates reference images for Figures 2–5, and independently checks the Figure 6 control described in S7. It is written as Supplementary_Code_S8_HEZ_Reproduction.py for Python 3 with NumPy and Matplotlib; the environment and plotting mesh describe this new independent implementation and are not attributed to the unspecified original software environment. For its deterministic analytic evaluations, a stochastic seed and ensemble size are not applicable.

Checks for Figures 2–5 include $\varphi(70\,\mu\mathrm{m}) = 1$, $r(70\,\mu\mathrm{m}) = 2$, $t(70\,\mu\mathrm{m}) = 0.5$, the reciprocal relation $r(x)t(x) = 1$ to numerical precision, the Lorentzian peak-height ratio $\frac{L(0;2)}{L(0;1)} = \frac{1}{2}$, and $\mathrm{FWHM}_u = 2r$. The companion code also reproduces the S7 matched-integrated-excess-damping area of approximately 96.2486 μm for anterior, uniform, and posterior reference kernels. With the specified 0.01-μm trapezoidal mesh, the computed anterior 0–150 μm fractions are approximately 0.9763005, 0.3333333, and 4.65×10^{-9}, respectively. These checks address numerical consistency of the chosen functions, not confirmation of a physical dissipation budget.

No corneal measurements, parameter estimation, optimization of x_0, dynamical Lindblad evolution, Keldysh noise simulation, reservoir-resolved entropy-production accounting, connected two-point density-correlation calculation, or hydrodynamic/Marangoni-like flow simulation is performed by this protocol. In particular, $\Gamma_{\mathrm{eff}}/\Gamma_{\mathrm{bg}}$ measures the imposed normalized spectral damping response, not physical entropy production. A correspondence between increased damping and shorter first-order amplitude correlations is therefore a conditional benchmark of the stipulated model. Independent depth-resolved measurements and a separately calibrated thermodynamic and transport budget remain necessary to evaluate the proposed HEZ and DDS hypotheses.

Supplementary Files

This is a list of supplementary files associated with this preprint. Click to download.

- SupplementaryMaterial.docx
- SupplementaryS7S8CodeReproduction.py.py